IMPACT OF LEIDENFROST DROPS ON SPHERICAL TARGETS

A THESIS SUBMITTED TO THE GRADUATE DIVISION OF THE
UNIVERSITY OF HAWAI‘I AT MĀNOA IN PARTIAL FULFILLMENT
OF THE REQUIREMENTS FOR THE DEGREE OF

MASTER OF SCIENCE

IN

MECHANICAL ENGINEERING

AUGUST 2018

By

Mitchel L. McLean

Thesis Committee:

John S. Allen III, Chairperson
Scott Miller
Weilin Qu

Keywords:
Leidenfrost drops, impinging drops, spherical target, experimental fluid dynamics, heat transfer

ACKNOWLEDGMENTS

First and foremost, I would like to thank my advisor, Dr. John S. Allen III, for his continued support, motivation, and patience. His dedication toward my success over the years has resulted in a remarkable amount of personal and professional development that I never assumed possible.

Beside my advisor, I would also like to thank my committee: Dr. Scott Miller, and Dr. Weilin Qu, for their insightful commentary and wisdom. I would like to further thank Dr. Miller for assisting with surface roughness measurements.

I would also like to thank the National Science Foundation grant #1542764 (Broadening Participation of Native Hawaiians for Engineering Faculty Careers), which provided me the opportunity to further my engineering education and research experience.

My work would not have been possible without the help of the University of Hawai‘i at Mānoa College of Engineering specialists: Mr. Lewis Moore and Mr. Caleb Pierick of the Mechanical Engineering department, and Mr. Mitchell Pinkerton and Mr. John Imai of the Civil and Environmental Engineering department.

In addition to being a supportive friend and colleague, collection of data would have been unsuccessful without the priceless expertise and assistance of Matsu Thornton, who helped me to build a versatile, reliable, and accurate heating control system.

I would like to thank my large network of family and friends who supported me through the last two years of my life. Many people came forward to help in every way they could, from sending me coffee and food to providing me a stable, affordable place to live. This work would not have been possible without the abundance of help I received from this large community.

I would also like to personally thank Lelemia Irvine and Sweetie Kuehu, whose wisdom helped me to survive graduate school, both mentally and physically, and kept me pointed in the right direction through the many challenges that were faced.

Lastly I would like to thank my girlfriend Christa, for her endless love and support through all the frustrations, challenges, and anxiety that could have otherwise derailed me from a successful path.

ABSTRACT

Johann Leidenfrost first proposed a physical explanation for the levitation of a water drop on a metal surface which was at a temperature well above the drop's boiling point. The drop floats above the surface and may be propelled vertically by the lateral flow of the vapor layer below. This phenomenon is known as the Leidenfrost effect. The Leidenfrost effect has been studied extensively for use in applications as well as its possible detrimental effects on heat transfer processes. Research advances have been made on impinging drops on superheated planar surfaces over the past fifteen years. The impingement of drops on spherical targets is less understood and this has important implications for petroleum processing such as in fluid catalytic cracking.

In this work, an experimental system was designed to heat metallic targets beyond the Leidenfrost temperature for drop impingement studies. Water drops with Weber numbers ranging from 10 to 45 were impinged on planar and spherical targets with temperatures from 160 °C to 220 °C. Impinging drops covered a larger surface area on a spherical compared to a planar surface. In addition, it was observed that the Leidenfrost temperature depended on the ratio of the drop diameter to the spherical target diameter. For Weber numbers from 10 to 15, drops were observed to rebound off the target. At Weber numbers from 15 to 30, hole formation was observed and analyzed. For greater Weber numbers and temperatures, liquid toroids were observed. The toroidal drop dynamics were measured with high speed photography and these results were compared with existing models for planar surfaces. The toroids broke up into a discrete number of smaller drops as a result of a Plateau-Rayleigh instability.

TABLE OF CONTENTS

LIST OF TABLES

LIST OF FIGURES

1 INTRODUCTION

1.1 The Leidenfrost Effect

1.1.1 History

In 1756, the German physician Johann Gottlob Leidenfrost provided the first physical explanation for the levitation of drops of purified water on an iron spoon which was heated until it was glowing [1]. Leidenfrost noted that the droplets would persist for minutes in this state and would maintain a spherical shape due to "mutual adhesion of the water particles among themselves," which would later be described as surface tension. Dr. Leidenfrost observed the evaporation of the bottom of the drop contributing to a pressure sufficient for levitation, subsequently known as the "Leidenfrost effect."

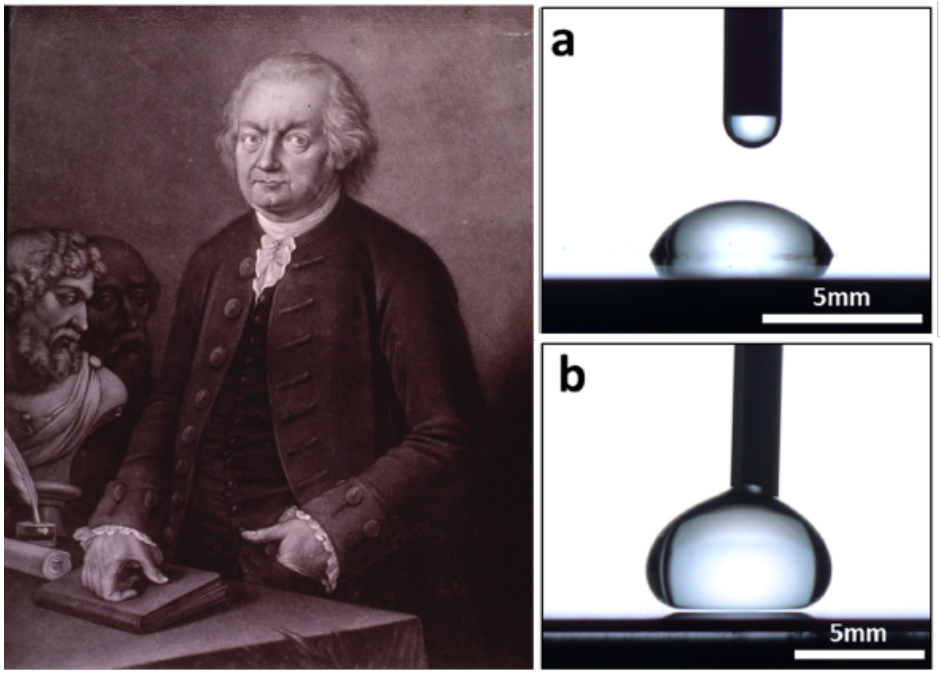

Figure 1.1. Left: A portrait of Dr. Leidenfrost by Gerhard J. Huck (1789) (source: US National Library of Medicine). Right: A drop placed on a surface at (a) 20 °C, and (b) and 250 °C (adapted from Geraldi et al. (2016) [2]). Note the vapor layer below the drop in (b).

It is likely that this phenomenon had been observed previously in the onset of the forging of metals. Hermann Boerhaave was the first to report the phenomenon in the literature in 1732, but did not give a complete physical explanation [1, 3]. Since the first scientific investigation by Leidenfrost in 1756, an abundance of research has been performed to understand the physics of

sessile and impinging drops on heated surfaces. To date, the Leidenfrost effect continues to receive attention as this topic is of both scientific and practical interest [4].

1.1.2 Boiling Regimes

The Leidenfrost effect has also been referred to as “film boiling” or “gentle film boiling.” This implies that a liquid drop levitates above a vapor layer beneath it. As shown in Figure 1.2, this is one of the four common boiling regimes. A sessile drop placed on a surface below its boiling point experiences evaporation without noticeable boiling. This type of boiling, called “film evaporation,” occurs at the liquid-gas interface. As the surface temperature is increased, the drop enters a boiling regime referred to as nucleate boiling. In this regime, vapor bubbles expand within the drop and reach the liquid-gas interface quickly. These may induce noticeable motion of the drop. As the surface temperature is further increased, it reaches a point at which the drop boils violently.

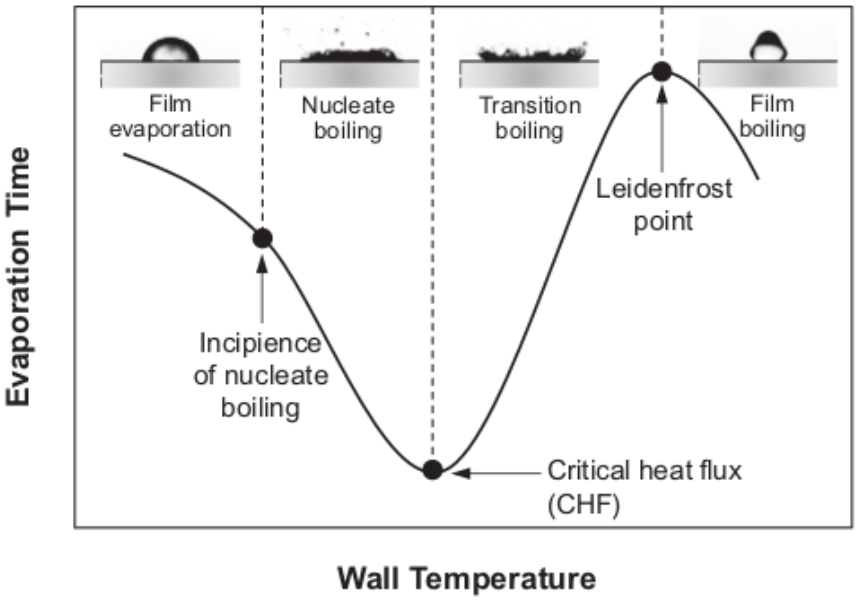

Figure 1.2. The different boiling regimes and heat fluxes as a function of the evaporation time for a liquid drop. Adapted from Liang and Mudawar (2017) [4].

As shown in Figure 1.2, the limit of the nucleate boiling regime corresponds with a Critical heat flux (CHF). At this temperature, the greatest amount of heat can be convected from the wall surface per unit time. Further increases in the surface temperature result in violent boiling with a marked decrease in the heat flux. This regime is referred to as the transition boiling regime, and its range extends to the temperature point of film boiling, also known as the Leidenfrost point. At surface temperatures near the Leidenfrost point, a sharp decline in heat flux occurs. At this stage, the liquid drop is no longer in direct contact with the surface, and the amount of heat removed

from the surface is limited by the conduction of the gaseous phase below the drop. Increasing the surface temperature further results in violent or chaotic film boiling with a corresponding increase in the heat flux. For water in a frying pan, the "film evaporation" regime corresponds to surface temperatures up to its saturation temperature of 100 °C. The nucleate boiling regime progresses uneventfully into the transition boiling regime. As a result, experimentally determining the temperature corresponding to the critical heat flux is challenging [4]. The Leidenfrost temperature for water in a frying pan is near 200 °C.

A related phenomenon of interest is the "inverse Leidenfrost effect." The inverse Leidenfrost effect occurs for a superheated object submerged in a liquid pool such that a vapor layer forms at the object's boundary. The inverse Leidenfrost effect was first described in the literature by Michael Faraday in 1828 [3].

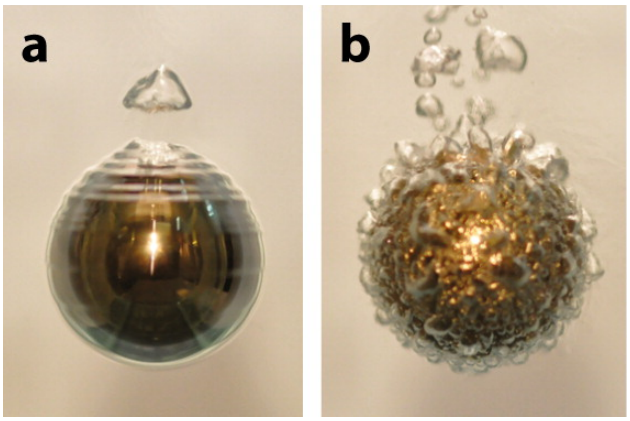

Figure 1.3. The inverse Leidenfrost effect (a) for a heated 15 mm diameter steel sphere in a liquid with a boiling point of 56 °C, and (b) transition boiling below the Leidenfrost temperature. Adapted from Quéré (2013) [3].

For example, spherical objects heated above their film boiling point may form a continuous vapor layer surrounding the object, and this can result in a considerable reduction in the force due to drag. As a result, the terminal velocity of the object in the liquid pool is greater than in the unheated case [5].

1.1.3 Industrial Applications

The Leidenfrost effect has been successfully shown to protect a human hand immersed in a pool of molten lead for a short period of time, though typically this is more of a demonstration than a practical application [6]. It has also been studied for its role in the injection of urea in exhaust gas streams from internal combustion engines [7]. The Leidenfrost effect can be detrimental to the removal of heat in cooling systems [8, 9, 10]. The greatly reduced heat flux in the film boiling regime may have catastrophic consequences in high-temperature applications in which the removal of heat is critical to the safe and/or efficient operation of a system.

Additionally, many metallurgical processes require the quenching of materials at various cooling rates. The inverse Leidenfrost effect can limit the available cooling rates for these processes [11].

One specific system in which the Leidenfrost effect may lead to disastrous consequences is a light-water nuclear reactor [12]. In the event of a power excursion, which is an unintended and uncontrolled fission reaction, superheated solid fuel in contact with water can be hot enough to be in the film boiling regime. The reduced heat flux in this regime may cause overheating; however, a more serious concern is that of vapor explosions. When the vapor film surrounding the solid fuel collapses as the fuel cools below the film boiling regime, the sharp rise in heat flux and subsequent vaporization of the surrounding water can quickly trigger large steam explosions. This interaction may have possibly occurred at the Chernobyl nuclear power plant disaster in 1986 [13]. Fluid catalytic cracking (FCC) is a process used in the petroleum industry to refine heavy hydrocarbons into lighter ones [14]. This emerging application of the Leidenfrost phenomenon involves the impingement of spherical drops onto heated spherical particles in petroleum processing [15].

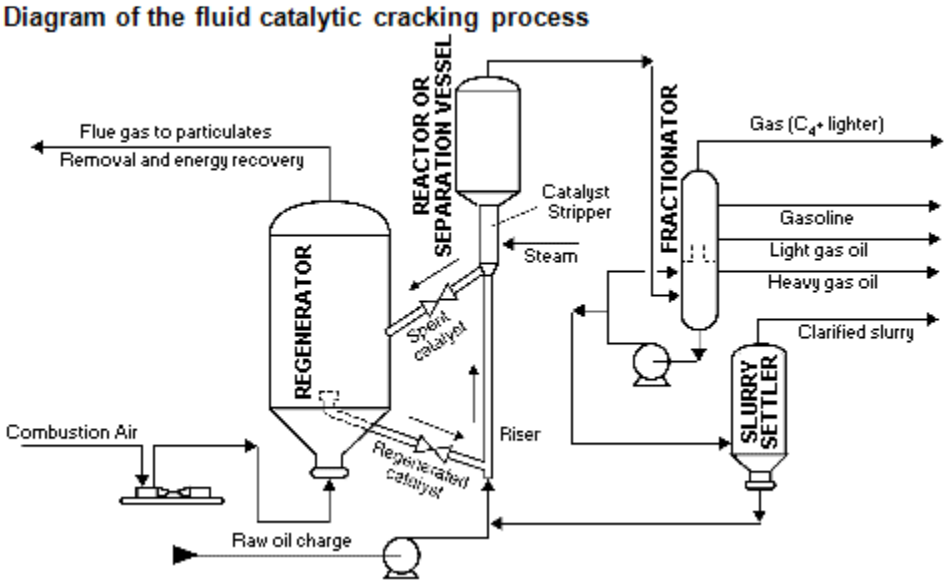

Figure 1.4. A diagram of a typical fluid catalytic cracking system (source: US Energy Information Administration).

In the FCC process, small fuel droplets impinge upon heated catalysts. The spreading of a thin film over a heated catalyst causes them to form lighter hydrocarbon chains. The incoming feedstock is atomized into a chamber containing catalyst particles, both of which are assumed to have diameters within an order of magnitude of each other. At this scale, an engineering approximation is made that both the impinging drop and the catalyst are spherical [15]. Interaction of spherical particles impinging on spherical catalysts in FCC processes is not well understood. This topic of engineering interest in part motivates this study.

1.2 Previous Research – Leidenfrost Effect

1.2.1 Overview

The Leidenfrost temperature and effect can be influenced by a multitude of parameters, including the fluid's chemical composition, the texture and geometry of the heated surface, gravitational forces, and any drop impact velocity. A drop may rotate and translate through alteration of the surface characteristics of the target [16, 17], including motion against the direction of gravity referred to in the literature as "jumping" [18]. It has also been found that the gravitational force can impact the Leidenfrost effect depending on its magnitude. Maquet et al. (2015) [19] found that increasing the effect of gravity through the use of a centrifuge resulted in increases in the Leidenfrost temperature. In terms of chemical composition, the Leidenfrost temperature can be increased for sessile drops through the addition of sodium and potassium salts in solution with distilled water [20]. The addition of a high alcohol content surfactant in solution with water was also shown to increase the dynamic Leidenfrost temperature [21]. There have also been investigations into the effects of chemical reactions between the impinging drop and heated surfaces [22]. For drop impact, the ratio of the drop to target size has a significant role [23].

1.2.2 Drop Impact: Planar Surfaces

The vast majority of studies on the Leidenfrost effect for impinging drops have been focused on planar surfaces [24, 25, 26] and their surface properties [27, 28, 29, 30]. A brief review is provided in this work, and a comprehensive review is given by Liang and Mudawar (2017) [4]. The main parameters that govern the behavior of the drop are density, velocity, characteristic length (diameter), dynamic viscosity, and surface tension. Results from the many studies relate drop impingement behavior to the Weber number, which relates the impinging drop's inertial forces to surface tension:

$$We = \frac{\rho v^2 l}{\sigma}. \tag{1.1}$$

In the case of an impinging drop with negligible initial velocity, g is the acceleration due to gravity, and h is the displacement from the drop's initial height to the contact surface. In this case, the Weber number can be expressed as:

$$We = \frac{2gh\rho l}{\sigma}. \tag{1.2}$$

A Reynolds number for this process is:

$$Re = \frac{\rho v l}{\mu} = \frac{\sqrt{2gh}\rho l}{\mu}, \tag{1.3}$$

which relates the inertial forces to viscous forces. Liang and Mudawar (2017) [4] highlight the distinction between the static and dynamic Leidenfrost temperatures. In the case of a sessile drop, the static Leidenfrost temperature is used. For drop impacts, vertical momentum influences the behavior of the drop after impact and a dynamic Leidenfrost temperature is needed. The dynamic Leidenfrost temperature is generally higher than the static Leidenfrost temperature, but becomes lower with increases in drop impact velocity and angle [4]. Figure 1.5 shows several key behaviors: drop rebounding, drop residence time (the amount of time the drop is in quasi-contact with the target), and the maximum spreading diameter. Leidenfrost drop impact on flat surfaces has been an active area of research in the last fifteen years [3, 4].

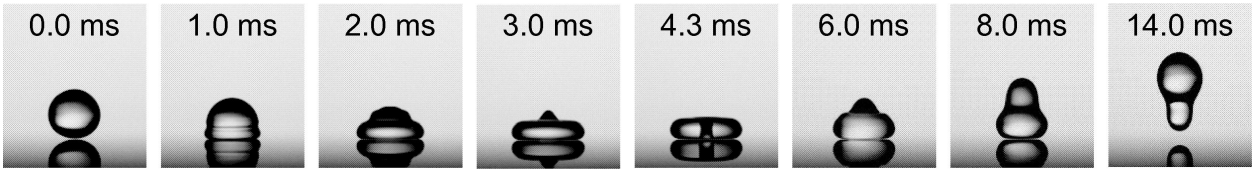

Figure 1.5. A butanol drop ($We = 4$) rebounding after impacting a surface superheated to 384 °C (after Liang and Mudawar (2017) [4]).

1.2.3 Drop Impact: Spherical Targets

Fewer studies have been performed on the impingement of liquid drops on unheated spherical targets [31][23][32]. Interactions of impinging drops on spherical targets above the Leidenfrost temperature are less understood. Banitabaei and Amirfazli (2017) [23] provide a review figure of previous and current work on drop impingement on both heated and unheated spheres. The figure includes various ratios of drop diameter to target diameter and includes recent work performed by Mitra et al. (2013, 2016) [15, 33] as shown in Figure 1.6 as "Ref.19," and "Ref.46," respectively.

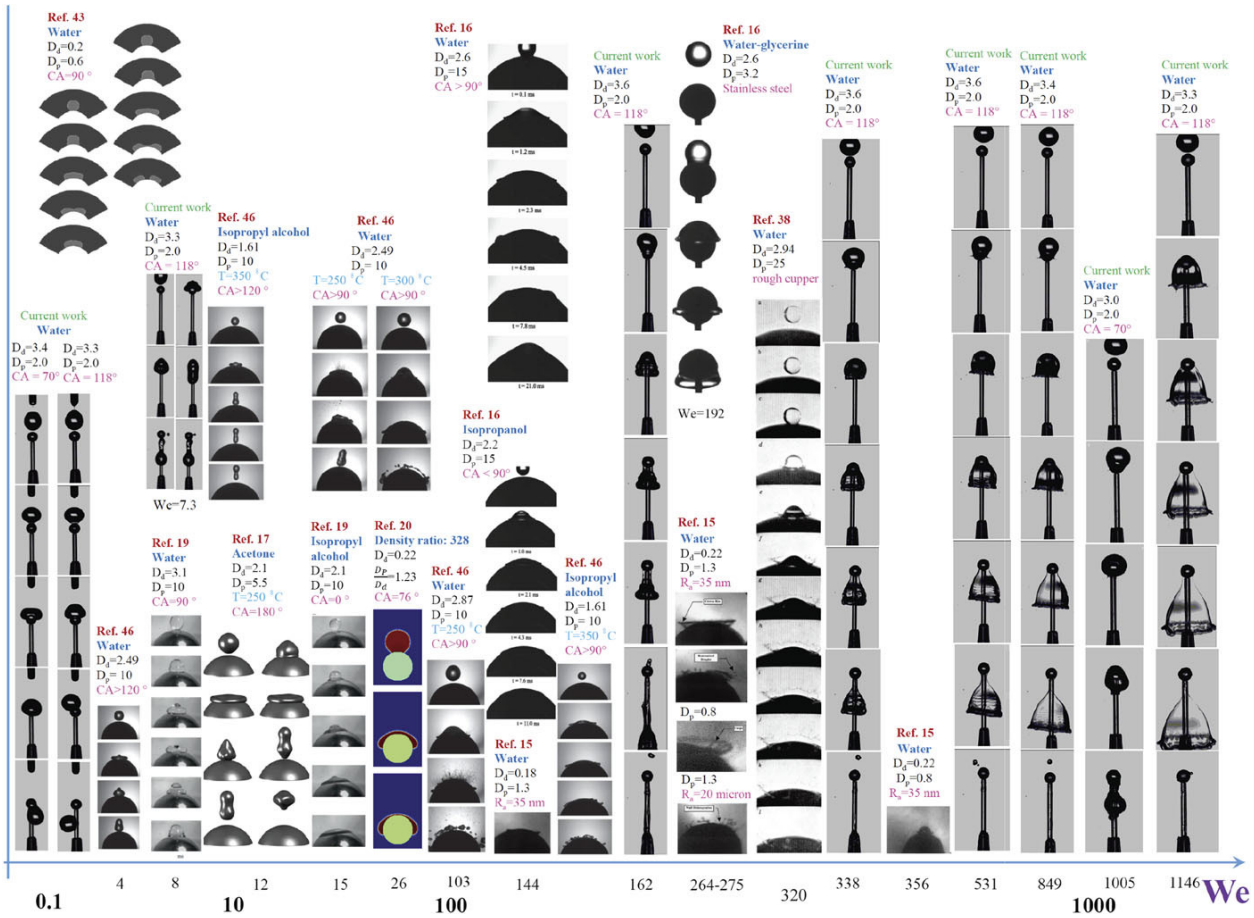

Figure 1.6. An overview of previous studies on drop impact on spherical targets for varying aspect ratios, temperatures, and Weber numbers (after Banitabaei and Amirfazli (2017) [23]).

Two distinct regimes for the impact of a spherical drop on a larger heated spherical target have been identified [15]. The first is a rebounding regime in which the drop hits the target and subsequently rebounds vertically as an elastic collision. The second regime involves the drop breaking upon impact into smaller drops. Mitra et al. (2013) [33] used a computational fluid dynamics model of a Leidenfrost drop impinging on a heated spherical surface to compare with experiments. In this work, the ratio of the drop diameter to the spherical target diameter was maintained less than unity. Mitra et al. (2016) [15] also provided an analytical model relating the ratio of the drop's maximum diameter after impact to its initial spherical diameter (which is referred to as the maximum spread ratio) to the drop's Weber number. We briefly describe these models as they are closely related to this work.

Figure 1.7 is a graphical representation of the drop impact as modeled by Mitra et al. (2016) [15]. This model assumes a mass and energy balance between two states: prior to impact and at maximum spreading after impact. At the first state, the drop is assumed to be spherical. At the final state, the drop is modeled as a volume contained within three surfaces: an upper portion in

contact with a surrounding gas, a lower portion in contact with the spherical target, and a perimeter portion in contact with both the spherical target and the upper surface of the drop.

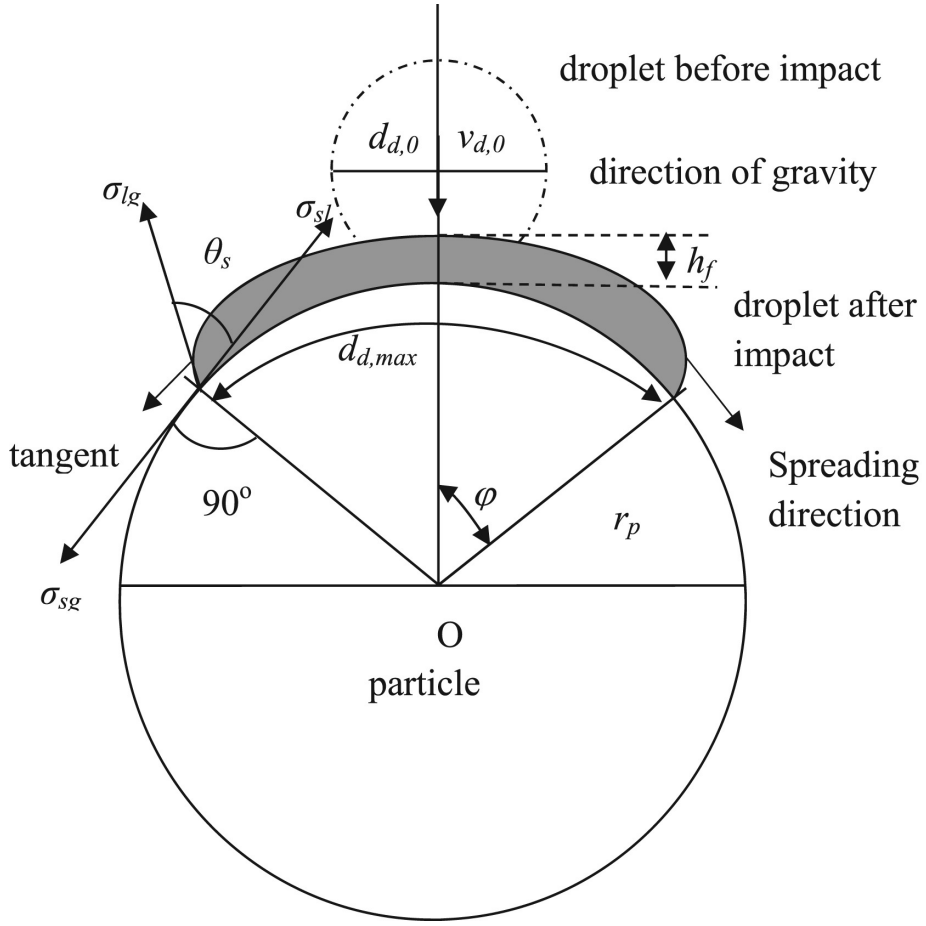

Figure 1.7. Spherical target impingement model (after Mitra et al. (2016) [15]).

Mitra et al. (2016) [15] compared this analytical model to an empirical relationship similar to that given by Araki and Moriyama (1981) [34] and found considerable disagreement between both models and experimental data, especially at higher Weber numbers. Mitra et al. (2016) [15] hypothesized that this discrepancy may be caused by the model's geometry, and that effects due to gravity may not be negligible at the nonzero angles of inclination.

The model (Mitra et al. (2016) [15]) assumes that the impinging drop is spherical. A liquid drop will maintain a spherical or quasi-spherical form if its radius is equal to or smaller than its capillary length L_c:

$$L_c = \sqrt{\frac{\sigma}{\rho g}} \tag{1.4}$$

which is equal to approximately 2.7 mm for liquid water [35]. Under the assumption of a spherical drop, the diameter can then be calculated from the drop's volume V as

$$d = \left(\frac{6V}{\pi}\right)^{\frac{1}{3}}. \tag{1.5}$$

However, in the Leidenfrost regime evaporation and fragmentation may occur, which are not accounted for in this model.

1.2.4 Drop Fragmentation and Toroid Formation

At low impact velocities, drops have been shown to rebound [4]. Above a critical impact velocity or Weber number, the drops break into many smaller drops. In the time between impact and break-up on planar surfaces, liquid torus shapes have been described [27]. The formation of liquid toroids from drop impact on heated planar surfaces has been previously investigated [27, 36]. Wu (2003) [36] showed that the maximum major diameter D (equivalent to $2c$ in Figure 1.8) and minimum sectional diameter d_{se} (equivalent to $2a$ in Figure 1.8) of a toroid can be computed analytically as a function of the impinging drop's diameter (d_l) and Weber number:

$$D = 0.48\left(1 + \frac{We}{12}\right)^2 d_l, \tag{1.6}$$

$$d_{se} = 0.66\frac{d_l}{1 + \frac{We}{12}}. \tag{1.7}$$

The study also showed that a critical Weber number exists, above which a toroid breaks up. The Weber number of this break up point can be calculated:

$$0.39\left(1 + \frac{We_c}{12}\right)^{\frac{3}{2}} + ln\left(1 + \frac{We_c}{12}\right) + ln\,(1.5) = ln\left(\frac{1}{r_a}\right), \tag{1.8}$$

in which r_a is the relative initial perturbation. Wu (2003) [36] noted that there is a large amount of uncertainty in choosing a value for r_a. Values used may include the average surface roughness of the wall or characteristic length of turbulence. The calculation of the critical Weber number is assumed to be insensitive to values of r_a. The results presented by Wu (2003) [36] were found to be in good agreement with prior experimental results.

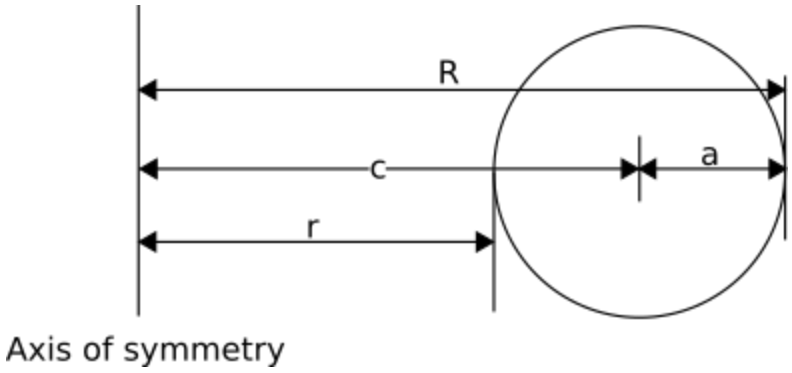

Figure 1.8. A cross section view of a single ring torus.

The break up of the toroid is reportedly due to a Plateau-Rayleigh instability [36], which has been studied for many decades for the breakup of a liquid stream or jet into droplets. This phenomenon is ubiquitous in everyday situations such as drops falling from a slowly leaking faucet. For engineering applications, it has also been used extensively for ink jet printing. A cylindrical flow with a free surface tends to minimize its surface energy by pinching and forming spherical drops. Wu (2003) [36] extended the instability to predict the breakup of a liquid torus on a flat plate and found that the critical Weber number for impact drop break-up was approximately 80. The generalization of the Plateau-Rayleigh instability theory to liquid toroids has not been fully established for spherical geometries. Moreover, the break-up of liquid toroids has been a topic of significant interest in recent years [37].

1.2.5 Thesis Research Outline

The dynamics of drop impact on heated spherical targets are not well understood. Fluid catalyic cracking has been described in the literature as a process modeled by drop impact on heated spherical targets [15]. The work done by Mitra et al. (2013, 2016) [15, 33] provides a preliminary, comprehensive study of drop dynamics for the impingement on heated spherical targets. Mitra et al. (2013) [33] includes a comparison between experimental data and computational fluid dynamics (CFD) simulations. Mitra et al. (2016) [15] provides relationships between the maximum spreading ratio. In addition, two main regimes were associated with drop impact on spherical targets: rebounding, in which the impinging drop bounces from the target, and break-up, in which the drop breaks upon impact into many smaller drops. It was found that these regimes were marked by a critical Weber number, below which drops rebounded, and above which break-up took place. Upon close inspection of these CFD results, we hypothesized that additional regimes may exist between the rebounding and drop break-up regimes.

Wu (2003) [36] described a torus shape which formed from drop impact on a planar surface. Relationships were given which relate the geometric properties of a liquid toroid to the impinging drop's Weber number. It was hypothesized that impingement of a drop on a spherical target may

be comparable to that of a planar surface such that Wu (2003) [36] analyzed. This has motivated the study of drop impact on spherical targets for the study of toroid formation. Additionally, the break-up of a toroid on a planar surface was shown to be influenced by a Plateau-Rayleigh instability, and related to the impinging drop's Weber number and diameter [36].

We will investigate the phenomena associated with Leidenfrost drop impact using primarily experimental methods with high speed video visualization and temperature measurements. Chapter Two outlines the experimental setup that was developed and implemented for this purpose. A custom temperature control system was implemented. Error analysis, uncertainty propagation, and heat transfer concerns are also addressed in this chapter. Chapter Three presents the results of the study for low (10-45) Weber numbers at temperatures between 160 °C and 220 °C. It was hypothesized that in this regime novel dynamics of drop impingement on heated spherical targets may exist.

2 EXPERIMENTAL METHODS

2.1 Experimental Setup

The purpose of the experimental study was to investigate the impingement of spherical drops on heated spherical targets. A fixed drop diameter smaller than the spherical target diameter was selected to relate to previous work and applications [15]. A system was designed for the acquisition of high speed optical data of impinging liquid water drops on heated metallic surfaces of different geometries. Some specialized and custom equipment were developed and used, as shown in Figure 2.1. In brief, a metal plate was fabricated to fix the spherical targets and allow heat to be conducted to them from below to attain specific surface temperatures. The metal plate was heated with power resistors. A Cognisys Inc. StopShot™ (Traverse City, MI) drop generator was positioned above the target to generate water drops of varying sizes. The properties of the distilled water used in experiments are given in Table 2.1. The drop size was calibrated to the variable pulse duration of the StopShot™ solenoid valve. A closed-loop feedback control system was built using an Arduino® (Turin, Italy) microcontroller to maintain the target's surface temperature which was measured by a thermocouple. A separate acquisition system was used to control the high speed video capture.

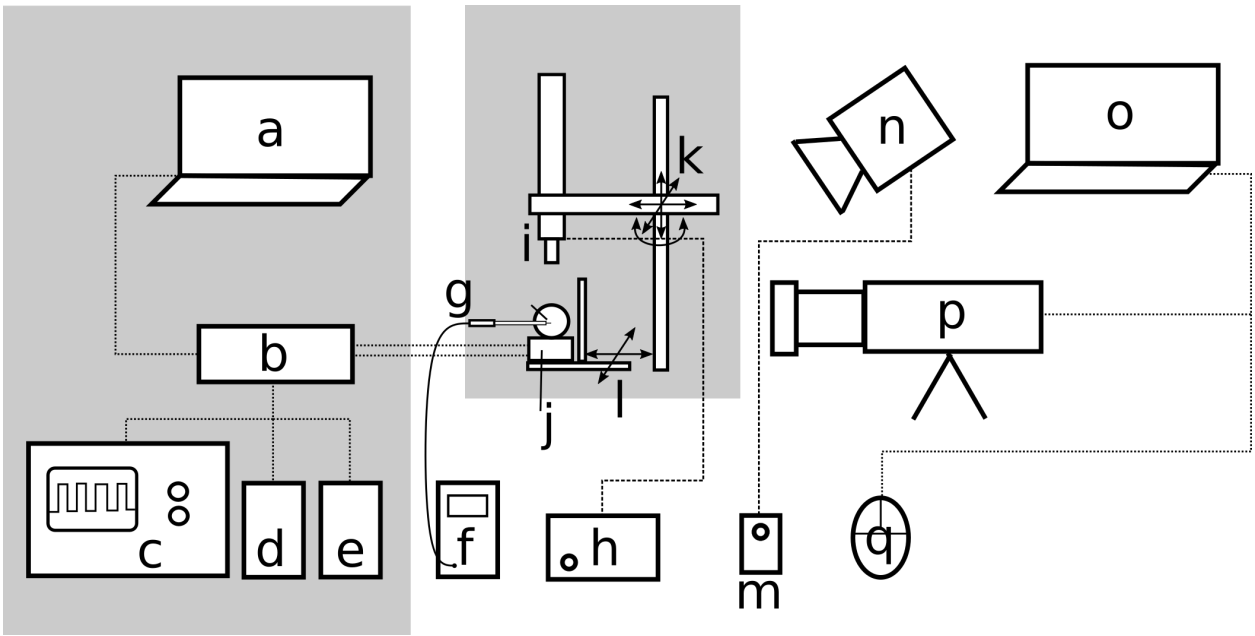

Figure 2.1. Experimental setup diagram.

Figure 2.1 shows the entire experimental setup. In the figure, two shaded areas indicate the heat control region (left), and a drop generation and target positioning system (center). An

Arduino® microcontroller (b) operated the closed loop proportional-integral-derivative (PID) feedback control of the current through the heater resistors in the heating plate (j).

Table 2.1. Physical properties of saturated water [38] [39].

Temperature ($^{\circ}C$)	Density ($\rho, kg/m^3$)	Surface tension ($\sigma, N/m$)	Dynamic viscosity ($\mu, kg/ms \times 10^{-3}$)
20	998.0	0.0727	1.002
50	988.1	0.0679	0.547

Control of the current to the heating block was accomplished by using an optocoupler and MOSFET with power supplies (d) and (e). The MOSFET gate voltage was set by (d) at 19.4 volts, while the voltage supplied by power supply (e) was set to 8.6 volts. Two resistors (Riedon® model UB5C-5R6F1) in a parallel configuration were supplied a power input of 22.3 watts, resulting in temperatures exceeding 325 °C within the heating block.

An oscilloscope (c) was used to inspect the waveform generated by the Arduino®'s PID control system for initial tuning. The setpoint and tuning parameters were programmed into the microcontroller using a designated laptop (a). A green LED was wired to the microcontroller and was programmed to turn on after the setpoint had been reached and the system was operating at steady state.

The drop generation and positioning components in Figure 2.1 (center shaded region) were needed for accurate target impact. The target (Fig. 2.1 g) was positioned directly below the drop generator nozzle (Fig. 2.1 i), which was controlled by its own StopShot™ controller (Fig. 2.1 h). Two optical positioners (Fig. 2.1 k, l) were used to adjust the target and nozzle positions in a horizontal plane for collinearity between the drop and spherical target centers. Both positioners were mounted to an optical table to provide rigidity and accuracy of measurements. The nozzle's optical positioner (Fig. 2.1 k) was also used to adjust the vertical position of the nozzle. For each experiment, the nozzle was lowered to the target surface and the height of the optical positioner (Fig. 2.1 k) was measured vertically from the optical table with a digital caliper. The digital caliper was then set to predetermined offsets for specific Weber numbers.

A digital thermocouple thermometer (Fig. 2.1 f) was used to verify the target's surface temperature. The right side of Figure 2.1 contains the optical system. An X-Stream VISION™ (Tallahassee, FL) XS-3 high speed camera (Fig. 2.1 p) was connected to a laptop (Fig. 2.1 o) to collect data. A high intensity light (Fig. 2.1 n) controlled with a wireless controller (Fig. 2.1 m) provided adequate lighting for the high speed photography.

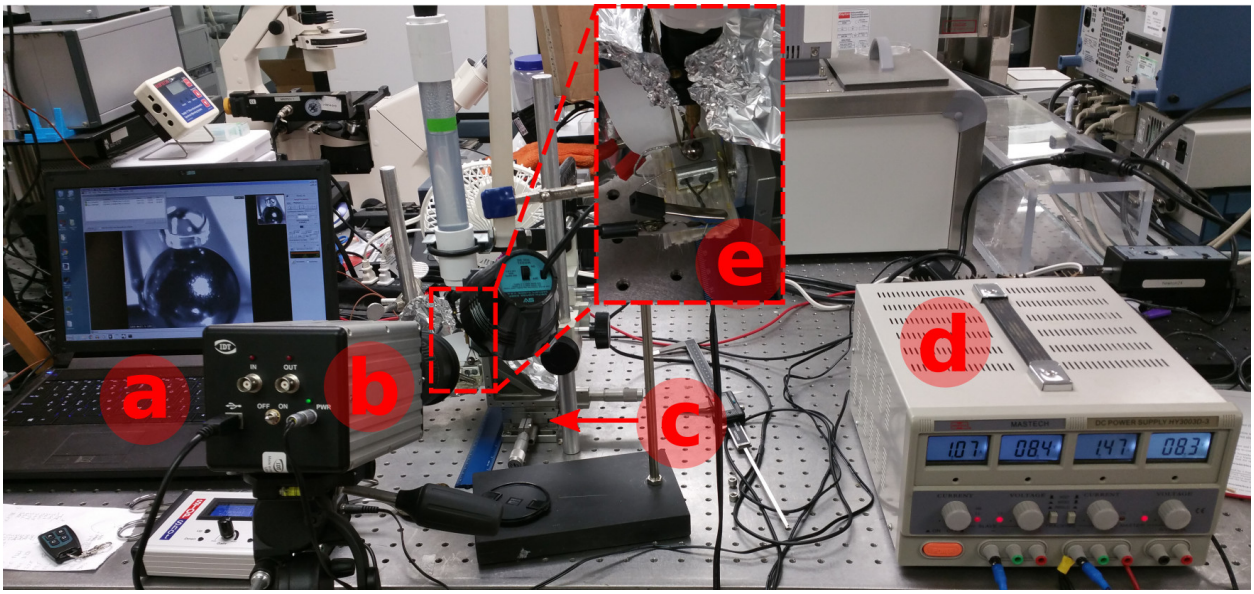

Figure 2.2. Experimental setup, includes (a) the computer control, (b) high speed camera, (c) target in positioning system, (d) heater power supply, and (e) zoomed view of the spherical target on the heating block, below the drop generator.

2.2 Experimental System Components

2.2.1 Drop Apparatus

The drop apparatus was a Cognisys Inc. StopShot™ water drop photography kit. The system included a liquid reservoir with an attached solenoid valve. The solenoid valve and reservoir were contained in a bracket. The included optical beam sensor was not used for triggering in these experiments. The nozzle affixed to the solenoid valve had a measured inner diameter of 3.99 ± 0.03 mm. The StopShot™ controller opened the solenoid valve for a programmable, variable pulse duration. The temporal resolution of the StopShot™ was set by the controller at 0.1 milliseconds.

A balance was used to determine the volume of liquid that the StopShot™ drop apparatus released per pulse. The StopShot™ was positioned over the balance. The pulse width duration was varied and the resulting drops were weighed. This data was analyzed with a linear fit which calibrated the StopShot™ pulse duration with the volume released. The laboratory conditions were approximately 20 °C and atmospheric pressure at sea level.

Through experimentation the minimum pulse width that reliably ejected a single drop from the apparatus was approximately 9.0 milliseconds for a drop diameter of 4.07 mm. The maximum drop diameter was limited by the drop's capillary length as in (1.4).

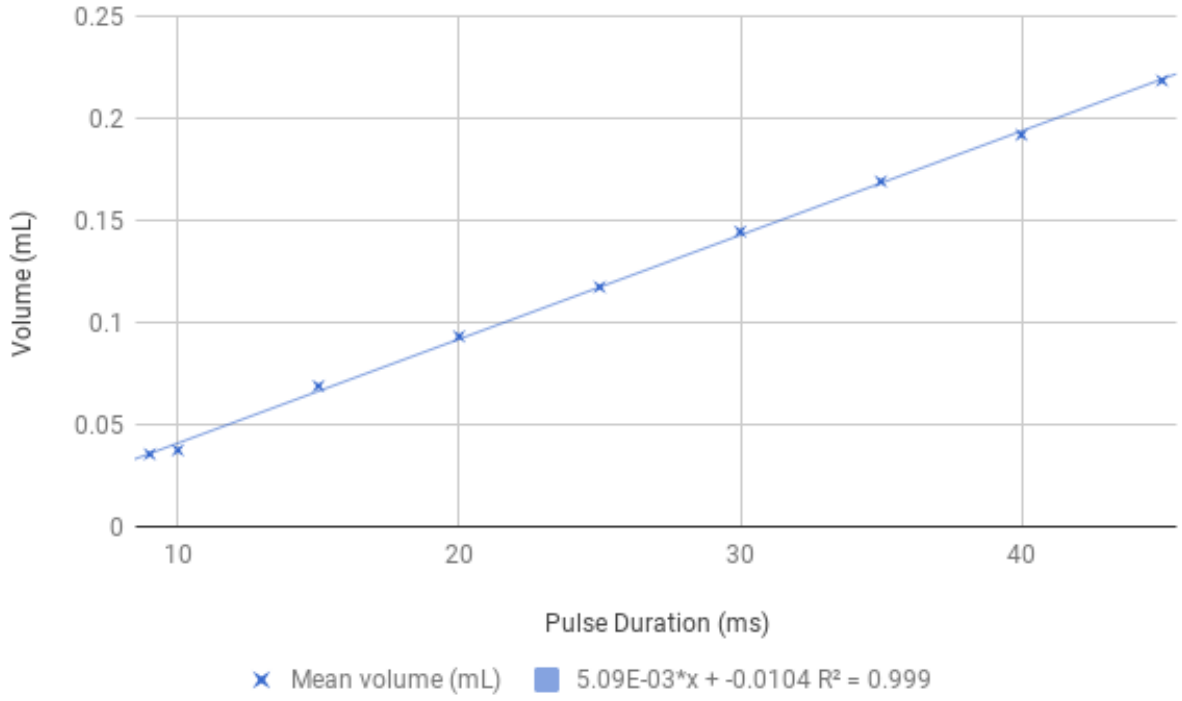

Figure 2.3. Drop volume (mL) calibrated with the drop apparatus pulse duration (ms).

The maximum drop diameter was calculated to be 5.40 mm, which equated to a maximum pulse width of 18.2 milliseconds. For convenience, the drop diameter and pulse width were fixed at 4.78 mm and 13.3 milliseconds, respectively. This restricted the drop diameter to target diameter ratio to 0.50 for the 9.56 mm diameter spherical target.

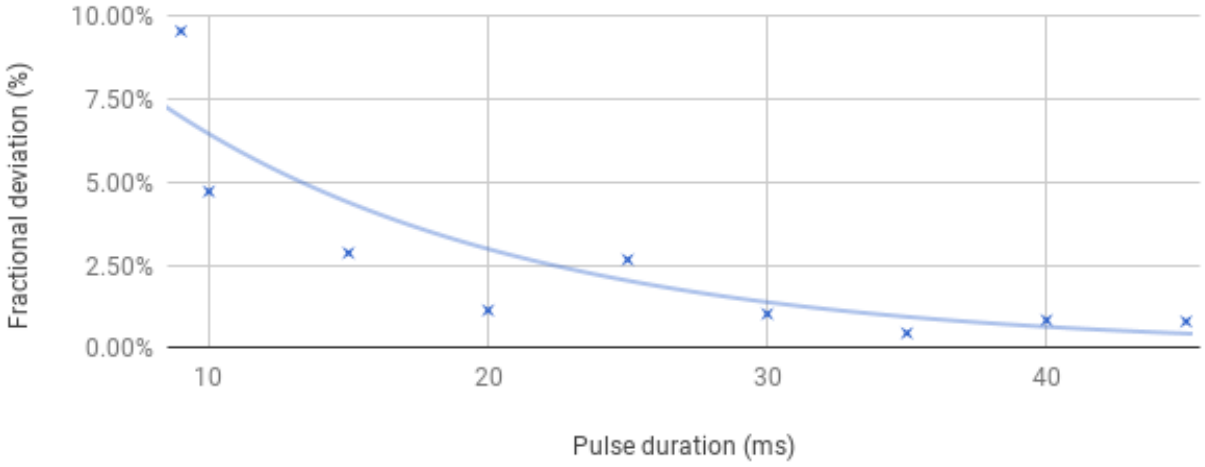

Figure 2.4. Relative deviation in volume for pulse duration.

Figure 2.4 shows the relative deviation for different pulse durations. For a fixed pulse duration of 13.3 milliseconds, the deviation was interpolated to be approximately 3 %, which was used in the calculation of uncertainty in the drop volume.

2.2.2 Heat Transfer System

In preliminary experimentation, an electric burner was used to heat a rectangular aluminum bar. The bar was machined to have small radial depressions ~O(3 mm) for holding the spherical targets. This method transferred additional heat to the StopShot™ nozzle which was measured by a mounted thermocouple. Temperatures as high as 60 °C were recorded. It was also observed that convection around the spherical target contributed to temperature fluctuations as measured by a thermocouple.

To address these concerns and improve the overall efficiency of the experimental test system, the electric burner was replaced with ceramic resistors in an improved system. An aluminum block (17.75 x 18.62 x 12.68 mm) was machined for two resistors to be placed inside it. The block was also machined to have a radial depression (1.82 mm radius, 0.26 mm depth) to keep spherical targets fixed. A flat depression was milled in the block to contain small spherical targets of varying sizes in a single layer packed configuration. This design facilitated the block and target to function as heat sinks for the resistors, thus allowing them to be operated in excess of their rated power limits.

2.2.3 Temperature Control System

The first iteration of the temperature control system used a relay to control the electric burner. This method of control involved only two states (on or off) which limited the available control scheme to Bang-bang control. This resulted in applying sufficient heat to acquire preliminary data, but oscillations about the temperature setpoint made data acquisition time consuming. Surface temperature measurements were taken manually and the acquisition sequence was initiated as the temperature approached the setpoint. This sequence was only performed when the temperature was falling from a temperature above the setpoint as a result of the heater being in its off state. This was carried out to reduce the heat flux from the electric burner to the target which was speculated to reduce convection. For improved data acquisition time and reduced heat flux to the surroundings of the experiment, a more efficient method to heat the target was needed. Moreover, a significantly improved system was designed to enable control of the heating element beyond two discrete power states. The resulting system that was developed was designed based on the closed-loop feedback diagram shown in Figure 2.5.

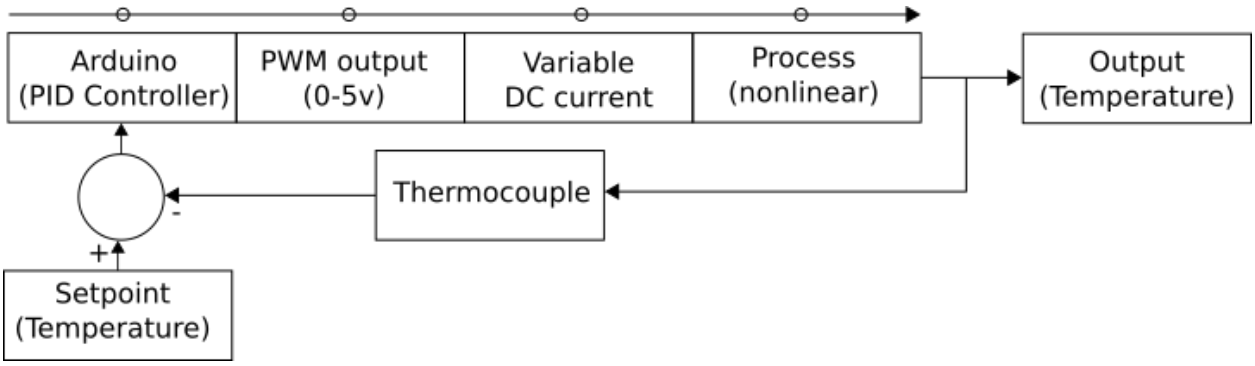

Figure 2.5. A simplified closed-loop feedback control block diagram.

An Arduino® microcontroller was used, along with its included PID libraries, to vary the output signal to a heating unit. The main loop of the microcontroller was as follows: A setpoint temperature was defined in the microcontroller code. The controller read a temperature measurement from a thermocouple via a PlayingWithFusion™ MAX31855 T-Type thermocouple sensor breakout board. The error between the setpoint and measured temperature was then used with functions provided by the PID library to determine an output signal. The output signal was limited to 256 discrete states due to the Arduino®'s 8-bit pulse width modulation (PWM) conversion. This output signal was then transmitted to an optocoupler which increased the signal voltage from a power supply. The higher voltage signal was then sent to the gate of a MOSFET, which had its other terminals connected to a DC power supply. This resulted in a variable current which was supplied to the ceramic resistors.

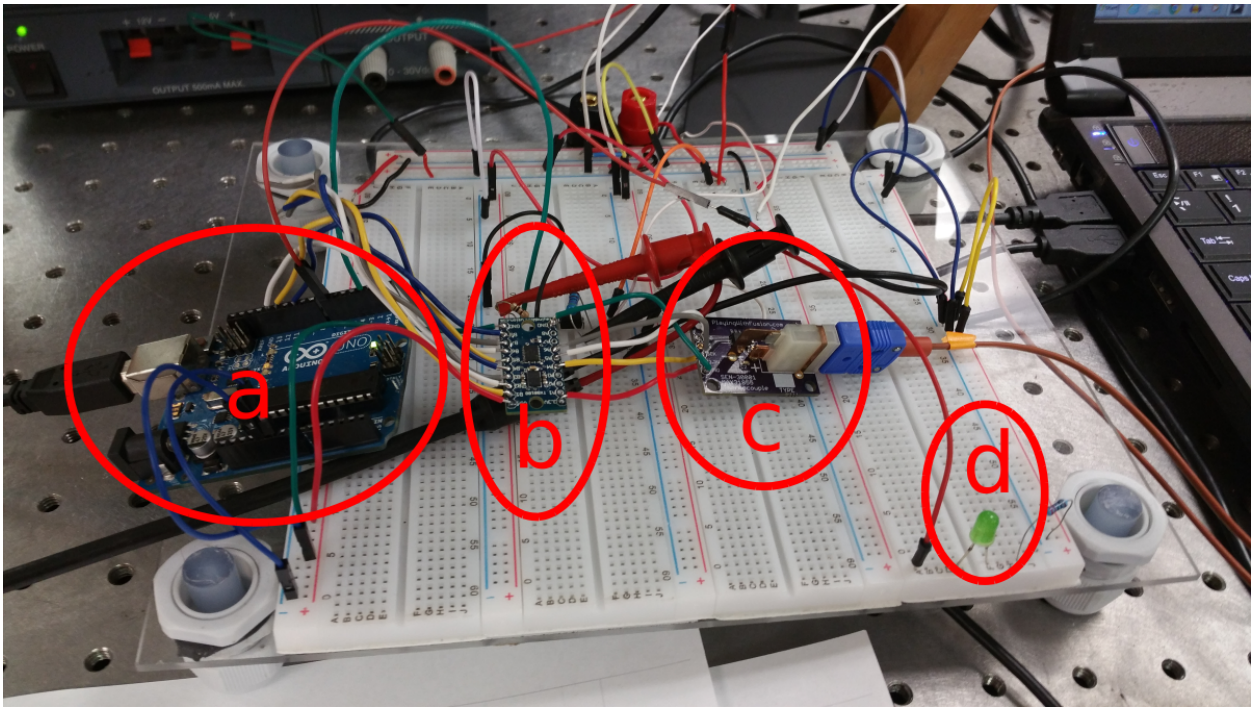

Figure 2.6. The PID control system, indicating (a) Arduino® microcontroller, (b) PlayingWithFusion™ logic level converter, (c) PlayingWithFusion™ MAX31855 thermocouple breakout, and (d) an LED turned on when the temperature reached steady state.

2.2.4 Positioning System

A custom positioning system was developed to precisely position the drop apparatus above the target. On the target side, a Newport 462 Series (Irvine, CA) two-dimensional crossed-roller bearing linear stage with an adjustment resolution of 1.0 micrometer was fixed to the optical table below. An aluminum channel L-bracket was bolted to the positioner to provide a table to secure the heating block to it. The drop apparatus itself was secured to a three-dimensional optical positioner. This provided for adjustment of the horizontal position of the drop as well as its height above the target.

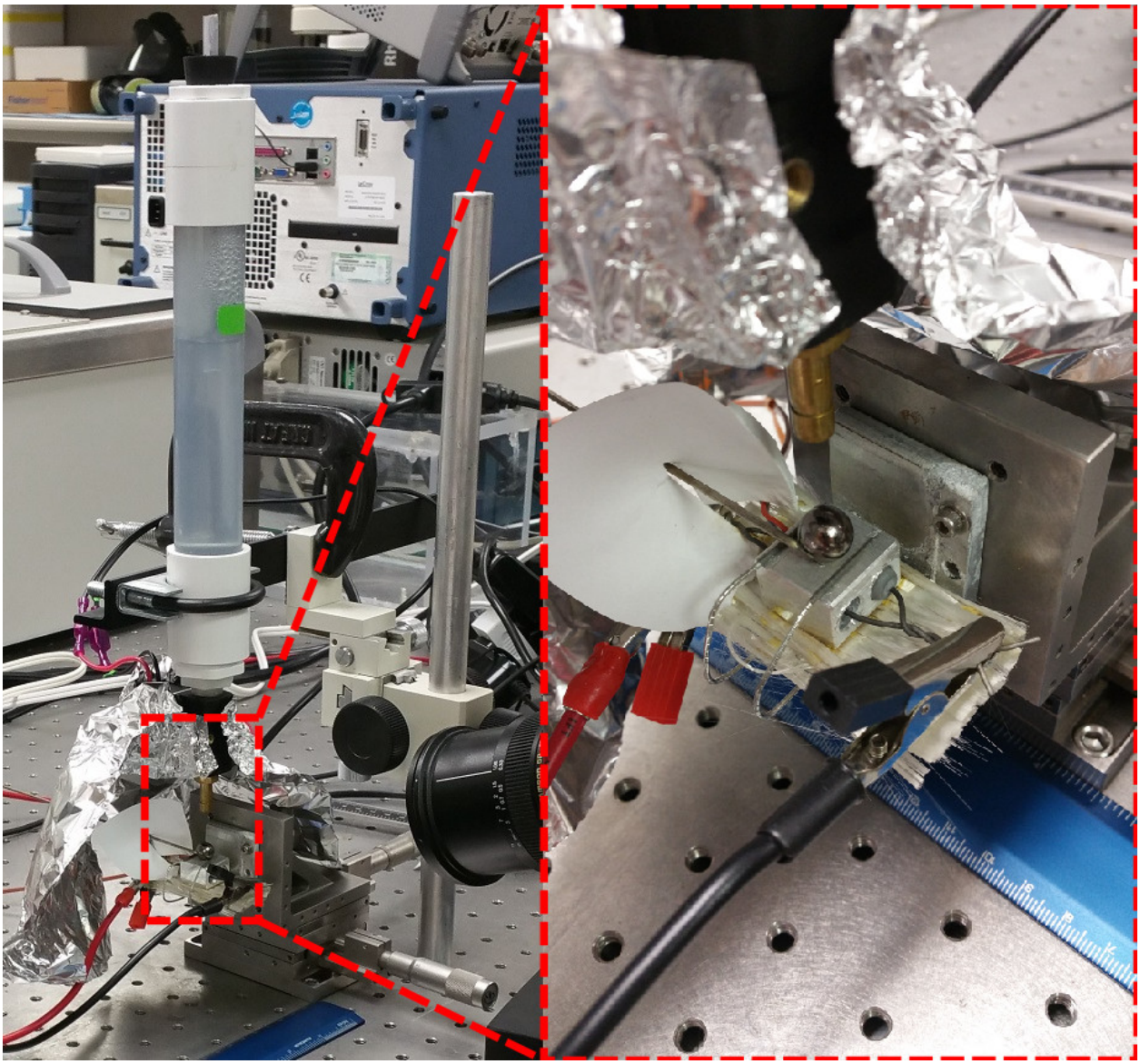

Figure 2.7. The positioning system and reservoir (left) and close-up view of the 9.56 mm diameter spherical target on the heated block (right). Aluminum foil was used to scatter light for the high speed photography.

The drop height was measured by first lowering the end of the drop generator nozzle until the tip was in contact with the target. The distance from a reference point on the optical positioner to the table was measured and recorded with a digital caliper (in depth mode). The height of the optical positioner was increased for another height measurement. The difference between the two measurements provided the drop height above the target. The uncertainty in measurement of the optical positioner offset was assumed to be the resolution of the digital caliper (100 microns).

2.3 Dimensional Analysis

The Buckingham π theorem was used to provide a functional relationship between a dimensionless time and the other variables. The time that an impinging drop contacts a heated surface was assumed to be a function of the drop's density (ρ), dynamic viscosity (μ), diameter (l), surface tension (σ), and velocity at contact (v). For this method, l, v, and ρ were selected as repeating variables and a total of three π groups were expected such that $\pi_1 = f\left(\pi_2, \pi_3\right)$. This resulted in the following π groups:

$$\begin{aligned} \pi_1 &= \frac{tv}{l} \\ \pi_2 &= \frac{\sigma}{\rho v^2 l} = We^{-1} \\ \pi_3 &= \frac{\mu}{\rho v l} = Re^{-1} \end{aligned} \tag{2.1}$$

which has the functional form

$$\frac{tv}{l} = f\left(We^{-1}, Re^{-1}\right) \tag{2.2}$$

For a flat plate, the residence time is often assumed to be on the order of the first vibrational mode of a drop [27]:

$$\tau_{osc} = \sqrt{\frac{\rho R_0^3}{\sigma}}. \tag{2.3}$$

This study is primarily on the impingement of drops on spherical targets, such that the dimensionless time in (2.2) was selected and found to be more appropriate.

2.4 Data Acquisition and Analysis

The surface temperature was measured by a digital thermocouple (Omega Fine Tip TJ Probe part number TJFT72-T-SS-116G-6-SMPW-M) (Egham, Surrey, United Kingdom) (Fig. 2.1 f). The microcontroller's LED remained lit when the heating block internal temperature reached steady state. A series of manual operations was then performed to capture data. First, a minimum of three drops were expelled from the StopShot nozzle (Fig. 2.1 i) into a metal spoon to ensure the subsequent drop size was not significantly reduced by evaporation from its free surface in contact with the air prior to release. Second, a photography light (Fig. 2.1 n) was switched on via its wireless controller (Fig. 2.1 m) to provide adequate lighting for the high speed camera. Subsequently, the high speed camera recording software was triggered by a mouse click (Fig. 2.1 q) immediately followed by the StopShot™'s pulse (Fig. 2.1 h). The data was collected for approximately two seconds. The data was then reviewed in the high speed camera software and saved.

All video data was obtained with the use of an X-Stream VISION™ XS-3 high speed camera. The software IDT Motion Studio was used to interface with the camera. The captured region of interest (ROI) was set to 256 by 256 pixels, allowing for a maximum capture rate of 2440 frames per second. The shutter speed was varied from 100 to 406 microseconds. Data from each experiment was analyzed manually using the software Tracker [40] and Fiji [41] (a distribution of ImageJ [42]). Reflections from the liquid surface resulted in gaps during binarization. A manual method was used for extracting critical features, such as the contact line of the drop on the sphere and the residence time.

A calibration tool in the software was used in each video to set a known length scale. This known length scale was used by the software to measure distances. For spherical targets, the known length scale was the diameter of the sphere. The flat disc was used as a model for impacts on planar surfaces.

2.5 Error Analysis

For the calculated Weber and Reynolds number values, the associated uncertainties from measurements were determined. Temperature measurements were made using thermocouples. These special limits of error (SLE) Tolerance Class 1 thermocouples result in a fractional uncertainty of 0.4%. Unless otherwise noted, all temperatures reported in this document carry this uncertainty with the exception of surface temperature readings.

Table 2.2. Measured quantities and their associated uncertainty.

Measured Quantity	Uncertainty	Unit
Temperature	0.4	percentage of reading
Displacement	0.03	mm
Fractional drop volume	3.0	percent

Figure 2.8 shows the output of the PID-controlled heater which maintains an internal setpoint temperature in the aluminum heating block of 280 °C. The blue and red lines represent a temperature of 1 °C above and below the setpoint, respectively. The time duration in this graph is approximately 50 seconds.

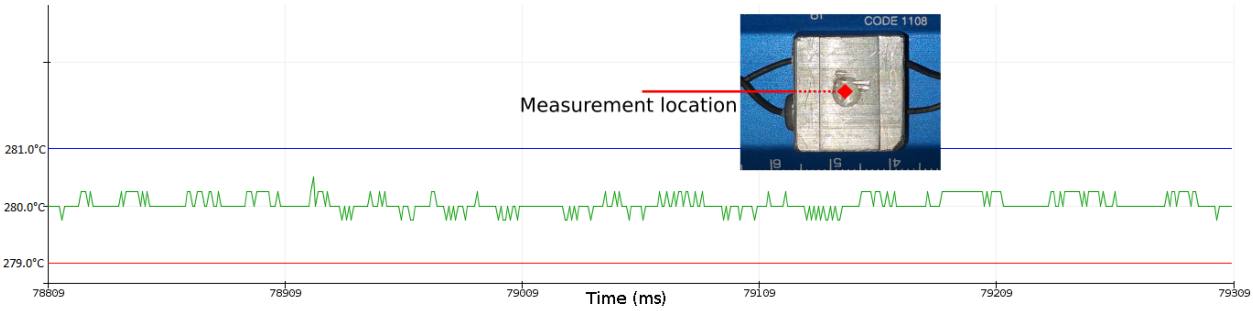

Figure 2.8. PID-controlled steady state temperature in heating block.

Figure 2.9 shows the fluctuating surface temperature of the spherical target, measured at its equator. We attributed these fluctuations to convection around the sphere, with a resulting standard deviation of 3 °C. Furthermore, another source of uncertainty is the assumption of uniform spatial surface temperature. The limits of this assumption were investigated by measurement of the surface temperature on the sphere's equator and at its north pole. An average temperature reduction of 4 °C was noted at the north pole compared to measurements along the equator. All surface temperature measurements for spherical targets were measured from the equator as to not interfere with the dynamics of the impinging drop.

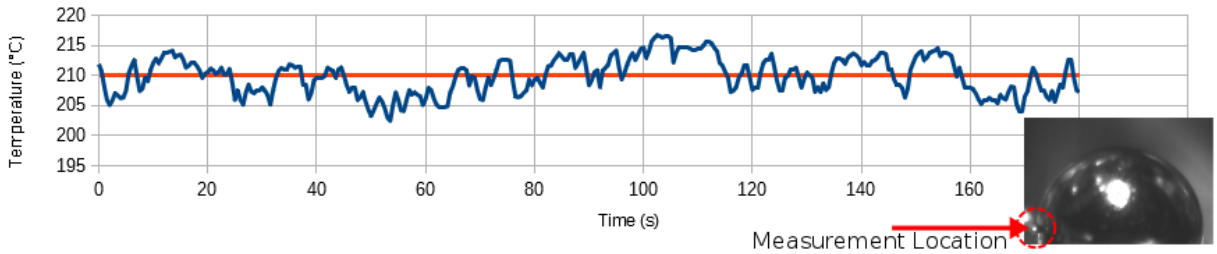

Figure 2.9. Spherical target surface temperature measurement.

The saturated liquid drops were assumed to be in thermal equilibrium with the solenoid valve nozzle. The temperatures measured with the thermocouples ranged from 20 °C up to a maximum of 50 °C, which corresponded to close proximities to the target. Due to these fluctuations, the fractional uncertainty in surface tension, density, and viscosity was taken to be the ratio of the difference in the properties at each temperature extreme to the lower value. This resulted in a fractional uncertainty of 0.066, 0.0099, and 0.454 for the fluid's surface tension, density, and dynamic viscosity, respectively.

Velocities used in the calculation of Weber and Reynolds numbers were derived under the assumption that the drop had no initial velocity. Under this assumption, and that the velocities in this experiment were low enough to neglect drag, the velocities were calculated as $v = \sqrt{2gh}$ where g was taken to be 9.81 m/s and h was the vertical offset from the bottom of the solenoid

valve nozzle and the target. In theory, the initial velocity of each drop was nonzero. However, due to the very short time scale involved in the pulse of the solenoid, a numerical approach would otherwise be required to determine the initial velocity. An alternative approach was performed using Tracker. The drop velocity immediately preceding impact was measured and compared to the theoretical values under the zero initial velocity assumption. The measured velocities were found to be in good agreement (under 2% difference) with the calculated values. Owing to the uncertainty associated with manual image analysis, this was an acceptable result and the zero initial velocity assumption was used for the calculation of all Weber and Reynolds numbers.

All measurements of length or displacement were made using a digital caliper with a measurement range of 0-200 mm, a resolution of 0.01 mm, and an accuracy of 0.03 mm. The uncertainty in the Weber number is:

$$\begin{aligned}
&\frac{\partial \sigma}{\sigma} = 0.066 \\
&\frac{\partial \rho}{\rho} = 0.0099 \\
&\left.\frac{\partial h}{h}\right|_{We=30} = 0.001 \\
&\frac{\partial l}{l} = \left|\frac{d}{dV}\left[\left(\frac{6V}{\pi}\right)^{\frac{1}{3}}\right]\right|_V \partial V \approx 0.414\frac{\partial V}{V} \approx 0.012
\end{aligned} \tag{2.4}$$

$$\frac{\partial We}{We} = \sqrt{\left(\frac{\partial \sigma}{\sigma}\right)^2 + \left(\frac{\partial \rho}{\rho}\right)^2 + \left(\frac{\partial h}{h}\right)^2 + \left(\frac{\partial l}{l}\right)^2} = 0.068. \tag{2.5}$$

The uncertainty in Reynolds number is:

$$\begin{aligned}
&\frac{\partial \mu}{\mu} = 0.45 \\
&\frac{\partial \rho}{\rho} = 0.0099 \\
&\left.\frac{\partial h}{h}\right|_{We=30} = 0.001 \\
&\frac{\partial l}{l} = \left|\frac{d}{dV}\left[\left(\frac{6V}{\pi}\right)^{\frac{1}{3}}\right]\right| \approx 0.414\frac{\partial V}{V} \approx 0.012
\end{aligned} \tag{2.6}$$

$$\frac{\partial Re}{Re} = \sqrt{\left(\frac{\partial \mu}{\mu}\right)^2 + \left(\frac{\partial \rho}{\rho}\right)^2 + \left(\frac{\partial h}{h}\right)^2 + \left(\frac{\partial l}{l}\right)^2} = 0.45. \tag{2.7}$$

For a Weber number of 45.0, this yields an uncertainty of ± 3.1. For a Reynolds number of 4000, the uncertainty is ± 1800. Although the uncertainty in the calculated Reynolds numbers was high,

the Weber number is the primary measure used for impinging drops. The Reynolds number uncertainty contributes to the uncertainty in the Ohnesorge number,

$$Oh = \frac{\sqrt{We}}{Re} = \frac{\mu}{\sqrt{\rho\sigma l}}, \tag{2.8}$$

which remains constant throughout experimentation for a fixed drop size. For completeness, the Ohnesorge number was calculated to be $(1.7 \pm 0.8) \times 10^{-3}$.

2.6 Target Properties

Two neodymium magnet targets were used: a flat disc and a sphere ($d = 9.56$ mm). The average surface roughness (R_a) of the plate was measured to be approximately 0.21 micrometers. The average surface roughness of the sphere was measured to be approximately 0.72 micrometers. Figure 2.10 shows the Sheiffield profilometer used to measure the average surface roughness of the targets. The spherical target was held in place with putty. The flat disc target was coated with nickel and the spherical target was coated with a black nickel. The average thickness of the coating in each case was reported by a manufacturer to be between 12 and 40 micrometers [43]. It was assumed that this thickness of the coating was negligible for the experiments and subsequent analysis. The targets were assumed to be homogeneous with the standard properties for neodymium magnets.

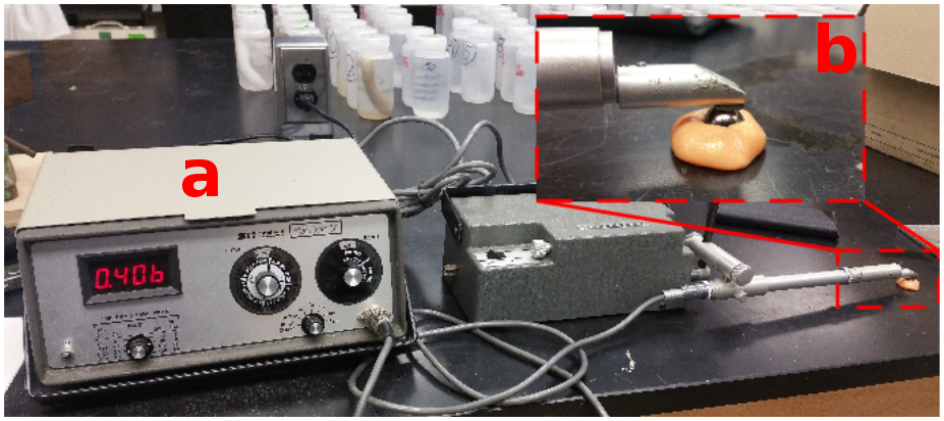

Figure 2.10. Spherical target surface roughness measurement (a), and close-up of the profilometer tip on the spherical target (b).

The target material properties are presented in table 2.3 for completeness.

Table 2.3. Properties of the neodymium magnets [43].

Target	Specific heat $(kJ/kg°C)$	Density $(\rho, kg/m^3)$	Thermal conductivity $(\kappa, W/mK)$	Mean surface roughness $(R_a, \mu m)$
Disc	0.50	7500	8.96	0.21
Sphere	0.50	7500	8.96	0.72

In order to assume a spatially uniform temperature for the sphere, the Biot number should be below ~0.1. The Biot number is

$$Bi = \frac{hL_c}{\kappa}, \tag{2.9}$$

in which h is the convective heat transfer coefficient, L_c is a characteristic length (the ratio of the volume to surface area), and κ is the thermal conductivity. The average Nusselt number for spherical geometries (Nu_D) is used to estimate the average heat transfer coefficient $\bar{h}_c$:

$$\overline{Nu}_D = \frac{\bar{h}_c D}{\kappa}, \tag{2.10}$$

in which D is the sphere diameter. The average Nusselt number has an empirical formulation

$$\overline{Nu}_D = 2 + \frac{0.589 Ra_D^{1/4}}{\left[1 + (0.469 Pr^{-1})^{9/16}\right]^{4/9}}, \tag{2.11}$$

for Prandtl numbers (Pr) greater than 0.5 [44]. The properties of air at 300 K were used in calculations such that the Prandtl number was 0.69. In order to calculate the average Nusselt number, the Rayleigh number is also used:

$$Ra_D = Gr_D Pr, \tag{2.12}$$

Gr_D is the Grashof number, defined as

$$Gr_D = \frac{\beta \Delta T g D^3}{\nu^2}, \tag{2.13}$$

β is the fluid's volumetric expansion coefficient, ΔT is the temperature difference between the object and the fluid, g is the gravitational acceleration, and ν is kinematic viscosity. Using the properties of the target in Table 2.3 as well as values of air at 300 K [44], the Grashof number was found to be 21030 and the Rayleigh number was calculated to be 14510. The corresponding average Nusselt number is 6.973. Solving (2.10) for $\bar{h}_c$ resulted in an average heat transfer

coefficient of 19.47 w/m^2K. Substituting these values and the properties of the spherical target into (2.9) yielded a Biot number of 0.0035 which is much less than 0.1:

$$Bi \approx 0.0035 \ll 1. \tag{2.14}$$

This supports the assumption of a spatially uniform temperature of the sphere for these experiments.

3 RESULTS AND ANALYSIS

3.1 Overview

In this chapter, we outline and discuss the results from the experimental setup described in Chapter Two. This study encompasses low Weber number ($10 \leq We \leq 40$) impacts of distilled water drops on flat and spherical targets with temperatures from 160 °C to 220 °C. The surface area of an impinging and spreading drop (with an initial diameter of 4.78mm) was compared between flat disc and spherical targets at 174 °C for Weber numbers of 17.4 and 21.4. An increase in the film boiling temperature was found for increasing drop diameter to target diameter ratios. We also studied the impinging drop behavior on a spherical target for Weber numbers between 10 and 30 and temperatures from 160 °C to 220 °C. The different drop dynamics and phenomena were characterized in terms of the temperature and Weber number.

3.2 Planar and Spherical Targets, and Drop Size

We investigated the observed Leidenfrost temperature and associated drop dynamics for impact onto a flat disc and onto a spherical target. From a preliminary investigation, we observed drop rebounding for the Weber numbers 17.4 and 21.4. A fixed surface temperature of 174 ± 3 °C was maintained for each surface. We used a drop with a diameter of 4.78 ± 0.06 mm. Differences in surface roughness between the targets was assumed to be negligible. The maximum spreading diameter of the drop on a flat target was measured across the drop as shown in Figure 3.2a. This measured diameter was used to calculate the surface area of the drop. For the spherical target, the cap parameter h was measured (Figures 3.1, 3.2b) and used to calculate the surface contact area of the drop. Three trials were performed for the two Weber number cases.

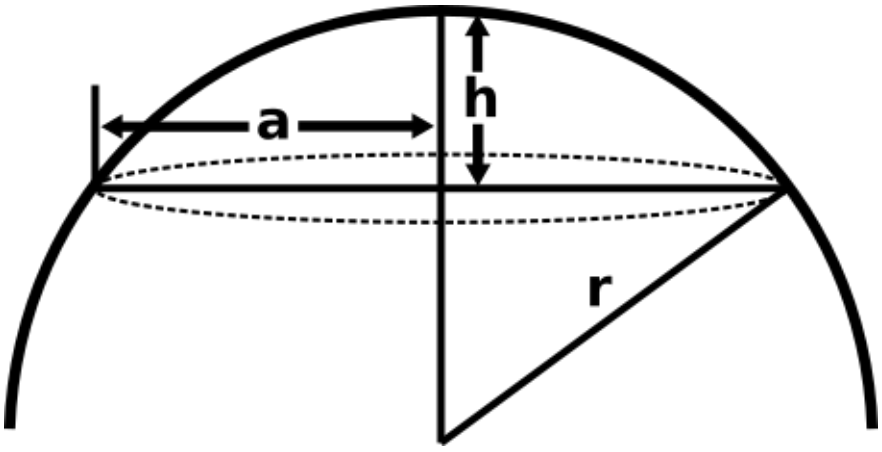

Figure 3.1. Spherical target and its geometric parameters.

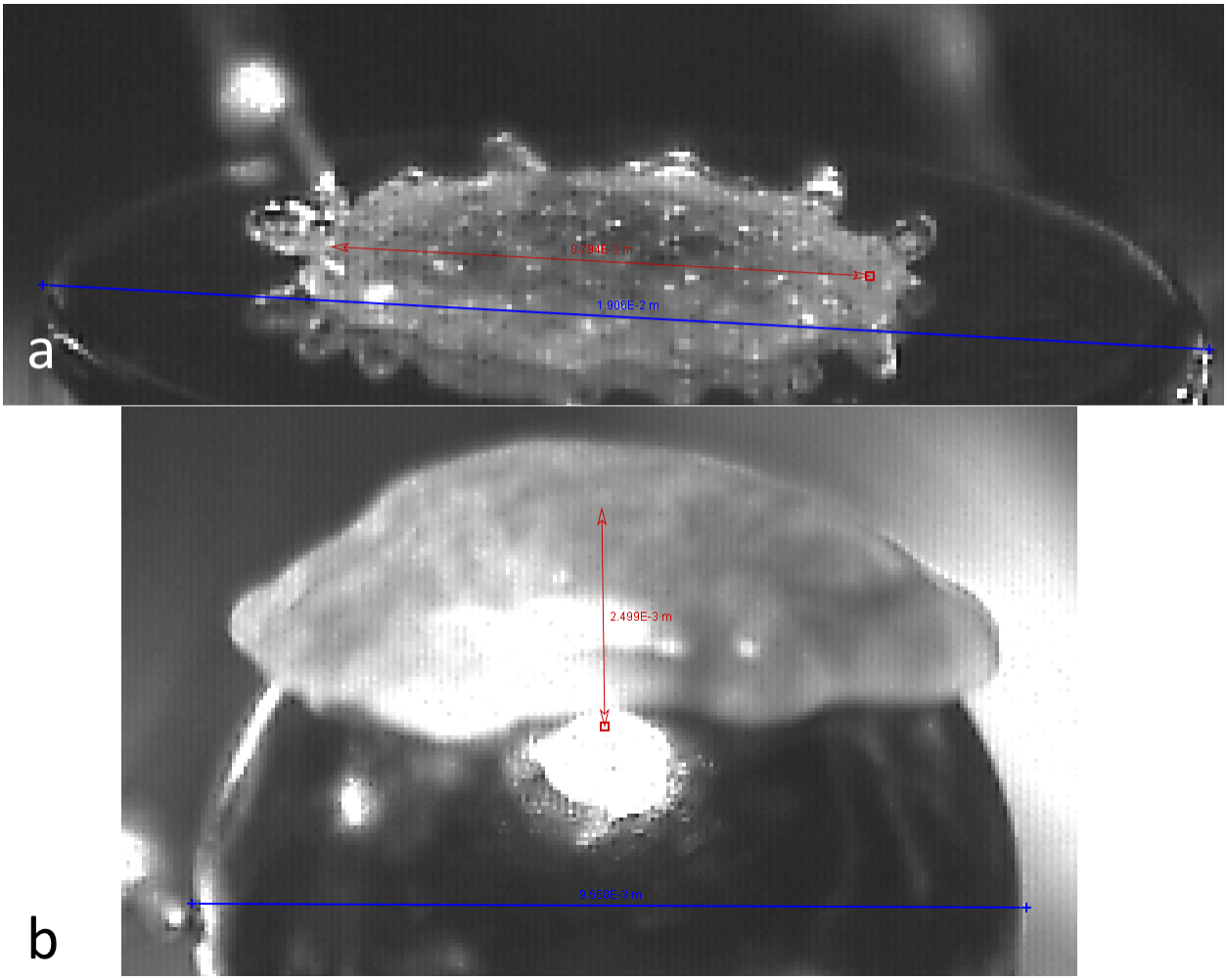

Figure 3.2. (a): Measurement of spreading diameter (red line, $d = 8.79$ mm) for flat disc with a calibration length scale (blue line, $l = 19.06$ mm). (b): Measurement of spherical cap height (red line, $h = 2.50$ mm) with a calibration scale (blue line, $l = 9.56$ mm).

A comparison was performed between the measured areas and the areas calculated by using the empirical equation for the maximum spread ratio on flat surfaces from Araki and Moriyama (1981) [34] and the analytical expression provided by Mitra et al. (2016) [15]; Table 3.1. The values obtained using Araki and Moriyama's empirical equation were in good agreement with the flat plate measurements. This was expected as the empirical relationship from Araki and Moriyama (1981) [34] was obtained for planar surfaces. However, noticeable differences arise at higher Weber numbers, which was mentioned by Mitra et al. (2016) [15]. The contact area that was obtained using the analytical solution for the maximum spread ratio on a sphere given by Mitra et al. (2016) [15] had better agreement at the higher Weber number. Table 3.1 summarizes the results of this investigation. An increased contact area was observed for the spherical target compared to the disc at both Weber numbers.

Table 3.1. Measured and calculated areas.

Target type	Weber number	Mean surface area (mm^2)	Standard deviation (mm^2)	Araki [34] %	Mitra [15] %
Disc	17.4	59.1	2.5	0.4	
Sphere	17.4	82.0	14.0	0.9	18.1
Disc	21.4	68.3	6.7	0.9	
Sphere	21.4	83.2	8.0	27.7	6.9

The ratio of the drop diameter to the target diameter was also investigated for temperatures ranging between 120 °C and 165 °C. This was accomplished by varying the drop size for the same sphere. In this series of experiments, the vertical height of the drop was fixed for various Weber numbers. The ratios 0.55, 0.60, and 0.65 resulted in Weber numbers of 142, 154, and 167, respectively. The results are shown in Figure 3.3.

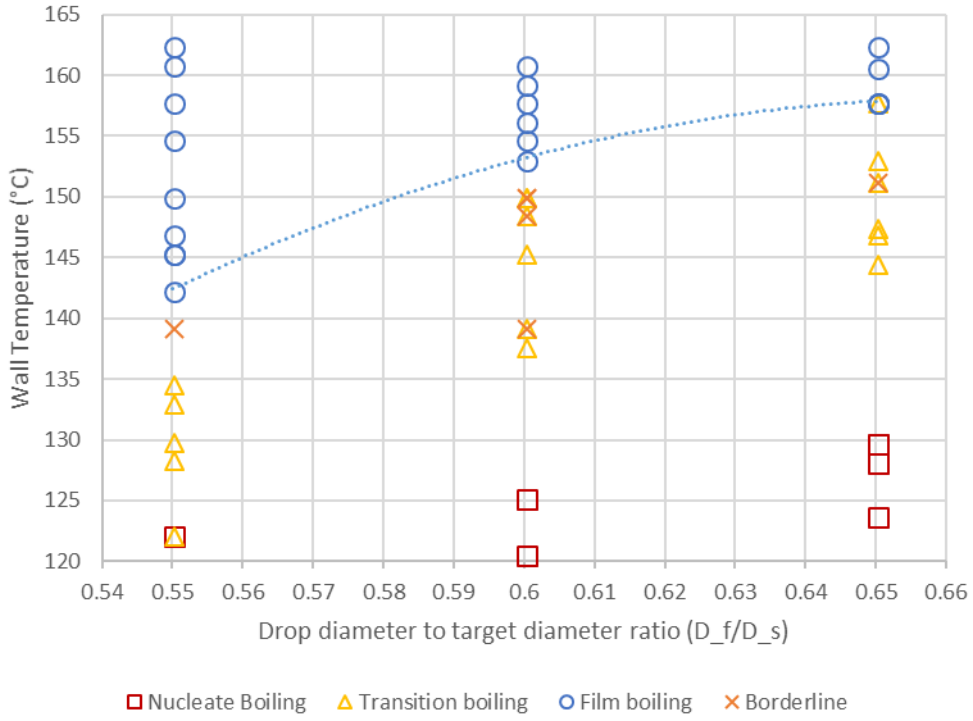

Figure 3.3. Boiling regimes for various drop diameter to target diameter ratios.

The three boiling regimes (Figure 1.2) are shown in Figure 3.3. Observations which were inconclusive were denoted as “Borderline.” The dashed line provides a visual aid to highlight the increasing film boiling temperature.

Mitra et al. (2013) [33] compared the measured maximum spread ratio on a spherical target to empirical and analytical relationships developed for the maximum spread ratio on planar surfaces. Figure 3.4 shows this comparison. We have included our work for temperatures from 205 to 220 °C and Weber numbers 10 and 12.5 with red stars in the shaded area of the figure.

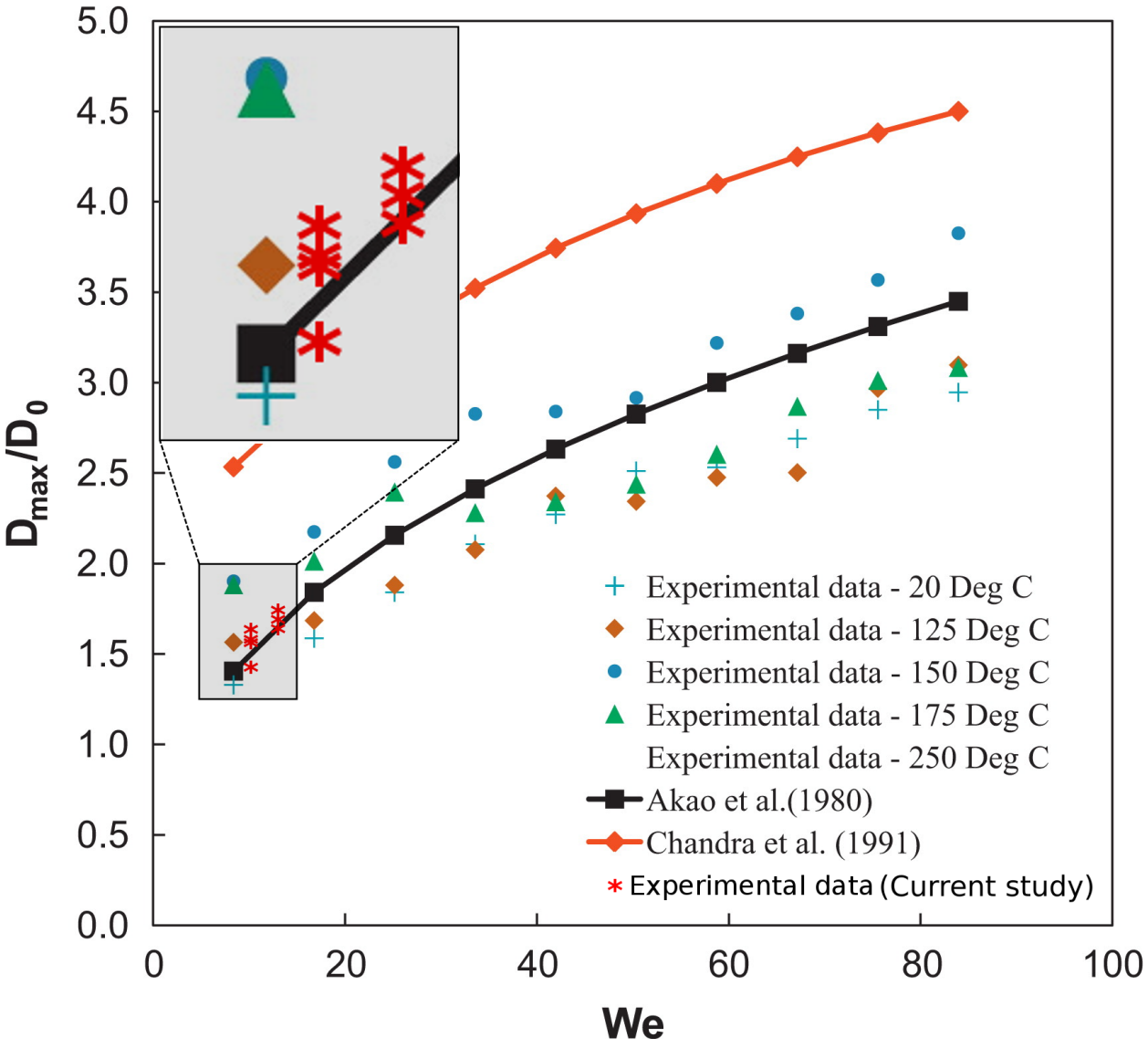

Figure 3.4. Data from this study and that of Mitra et al. (2013) [33]. Work from the current study is shown in the shaded area with red stars.

3.3 Drop Rebound, Hole and Toroid Formation

An investigation into the behavior of impinging drops for temperatures ranging between 160 °C and 220 °C was performed with Weber numbers ranging from 10 to 30 as shown in Figure 3.5. Four distinct physical phenomena were observed, which are discussed in separate sections.

- **Rebound**: Drops spread to a maximum diameter, recoil, and either bounce or slide off the surface
- **Hole Formation and Closing**: A hole is formed during the drop spreading phase which subsequently closes
- **Toroid**: A hole is formed during the drop spreading phase which remains open, thus forming a toroid; the toroid subsequently breaks up into a discrete number of smaller drops
- **Non-toroidal Break-up**: A hole is formed during the drop spreading phase which does not result in a toroid and subsequently breaks up asymmetrically

Figure 3.5 summarizes the drop dynamics in terms of temperature and Weber number. The rebound regime was observed for temperatures below 195 °C at all Weber numbers, and for Weber numbers below 20 for all temperatures. The hole formation and closing regime (denoted as "Hole closing" in Fig. 3.5) was seen sporadically prior to the onset of toroid formation or non-toroidal break-up. Non-toroidal break-up was seen at a temperature preceeding toroidal formation for each Weber number. Toroids developed for Weber numbers greater than 12.5, and for surface temperatures above 190 °C. The transition region between drop rebounding and toroid formation is shown as the curved shaded area of Figure 3.5.

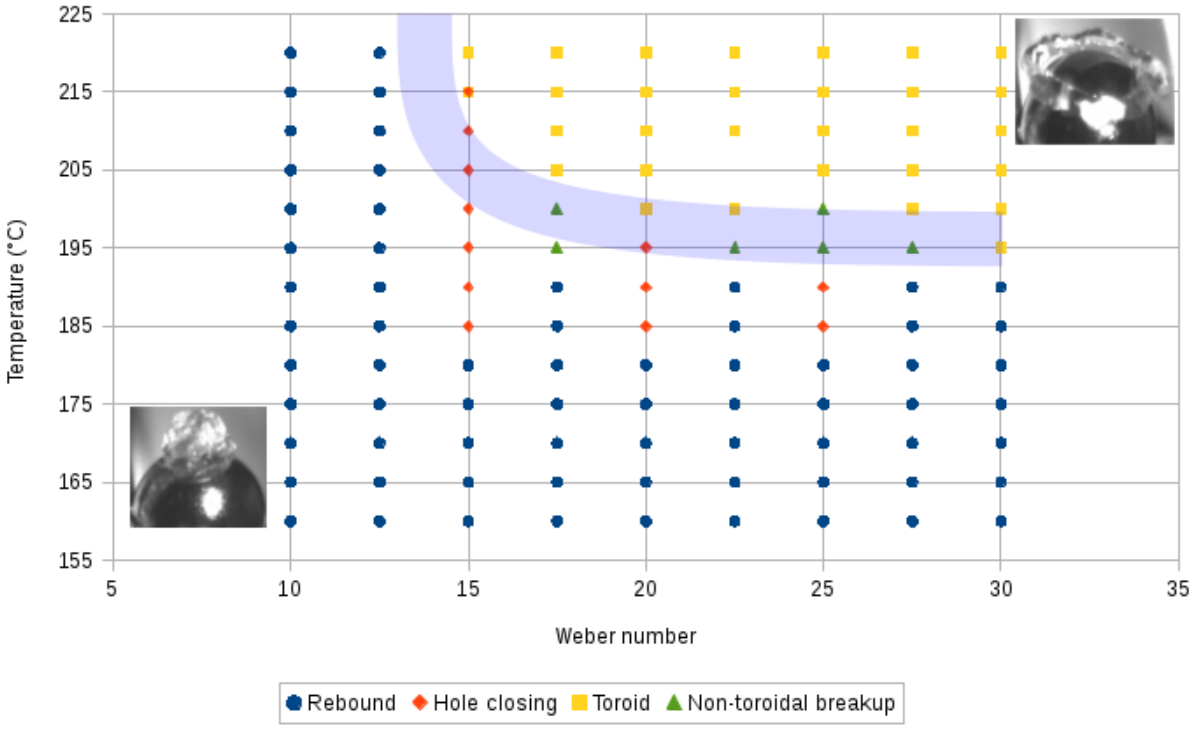

Figure 3.5. Drop regimes for spherical target impingement.

3.3.1 Rebounding

Drop rebounding is characterized as a partially elastic collision between the drop and a target. A rebounding drop bounces off of the target after what is known as the "residence time" [4]. The residence time scales with We^{-1}.

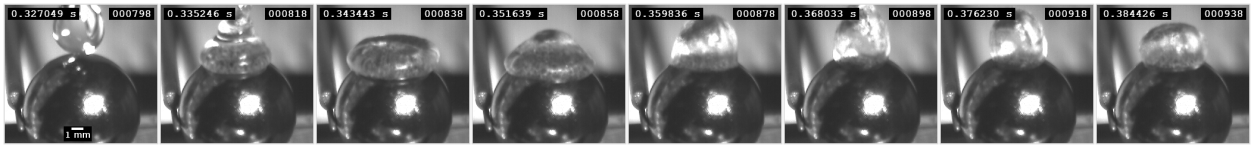

Figure 3.6. An impinging drop at a Weber number of 10.0 and surface temperature of 210°C. The drop oscillates upon impact and in this case remains on the target surface.

Drop rebounding residence time was studied for the Weber numbers 13.6, 17.4, 21.4, and 22.8. Hole formation was observed at a Weber number of 22.8. The data shown in Figure 3.7 was fit to a model (3.1).

$$t^* = aWe^b \tag{3.1}$$

The variables a and b were found through regression techniques. The values obtained were $a = 64 \pm 105$ and $b = -0.98 \pm 0.60$ for the 95% confidence interval.

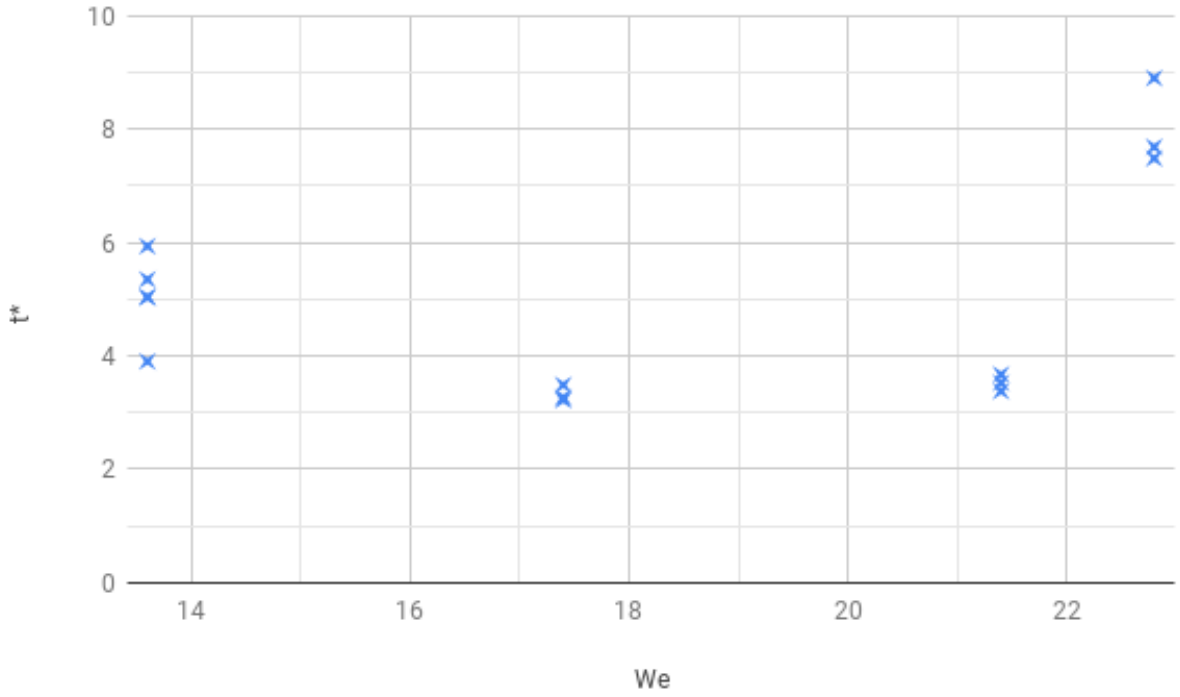

Figure 3.7. Dimensionless residence time for drops rebounding at 174 °C (Weber numbers 13.6, 17.4, 21.4, and 22.8). A decrease in residence time occurs from Weber numbers 13.6 to 17.4. Hole formation was observed at a Weber number of 22.8.

Figure 3.8 shows hole formation for a critical Weber number. A difference between these two cases is the formation of a hole and the decreased vertical rebound of the drop.

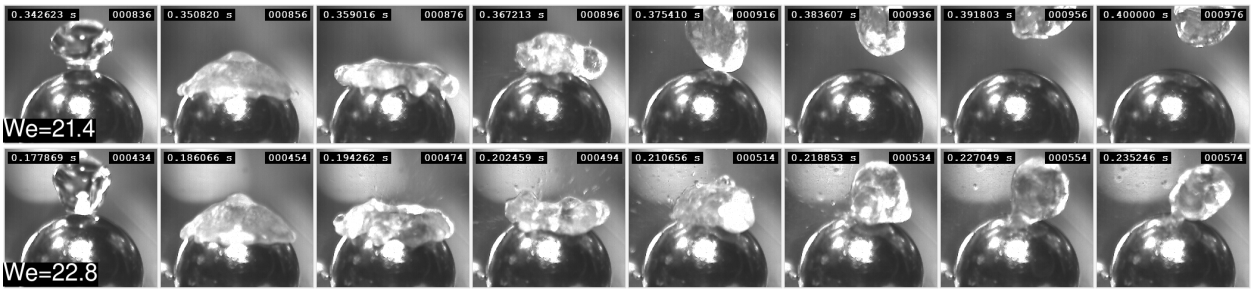

Figure 3.8. Top: A drop with a Weber number of 21.4 impinging on a sphere (T=174 °C), which rebounds off the surface. Bottom: A drop on a sphere of the same temperature with a Weber number of 22.8 forms a hole and has a reduced rebound.

3.3.2 Hole Formation

Two distinct hole formation regimes were noticed. Typically at higher Weber numbers a hole was observed away from the north pole of the sphere. This thin spreading region was shown by

Zhu et al. (2017) [32]. At lower Weber numbers and higher surface temperatures, hole formation was seen to initiate at the north pole of the spherical target. In this regime, the hole subsequently closes, resulting in either oscillation or partial rebound. Figure 3.8 shows different behavior when this type of hole is formed and closes. This phenomenon was observed for a Weber number of 40.0 for a surface temperature of 220 °C in Figure 3.9. The hole expands to a maximum diameter of approximately 3.0 mm before the coalescing and closing.

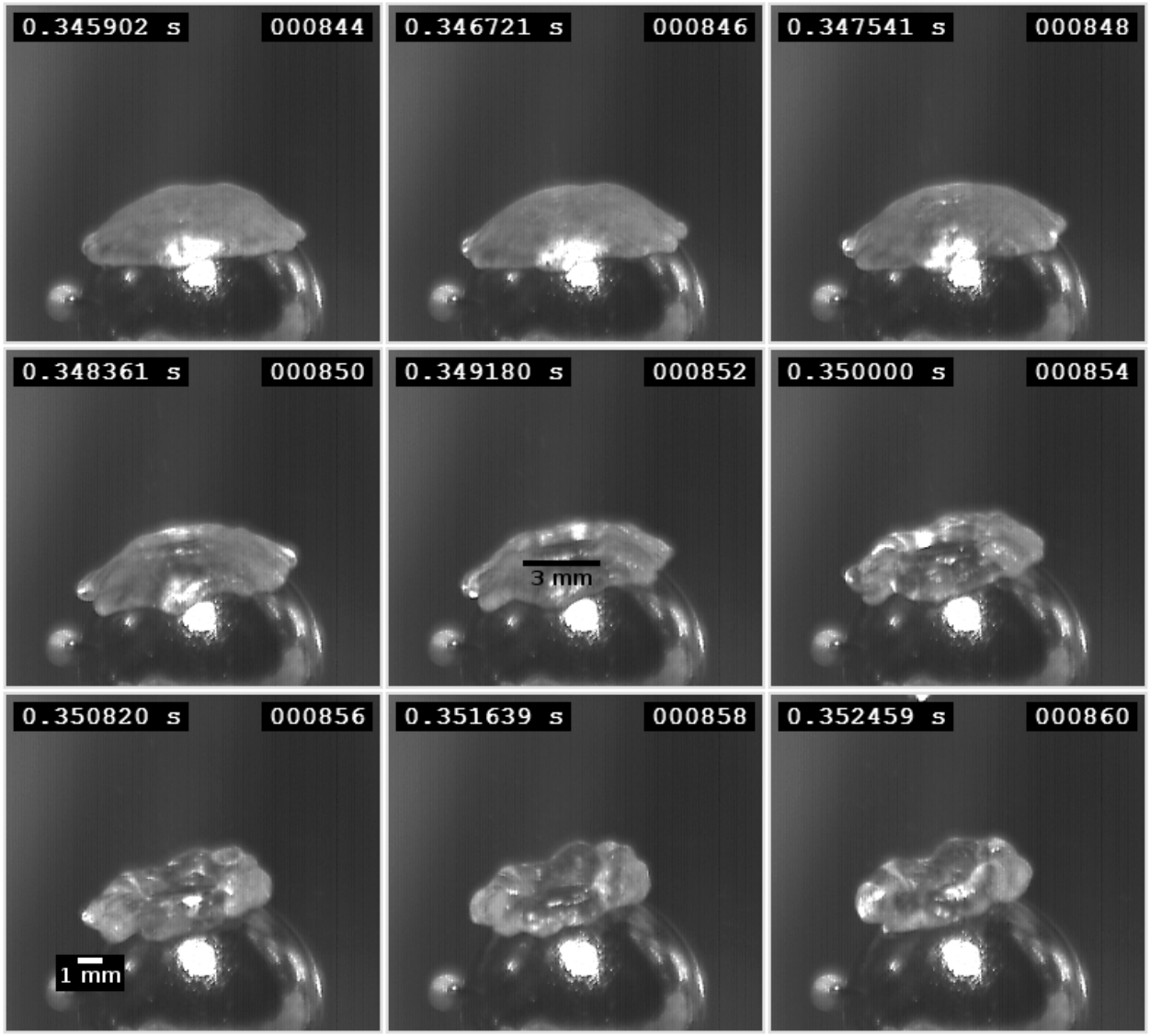

Figure 3.9. The formation and subsequent closure of a hole of (~3 mm) at a Weber number of 40.0 and a target surface temperature of 210°C.

The motion of the drop contact line was analyzed using Tracker. Figure 3.10 shows the measured vertical position and velocity.

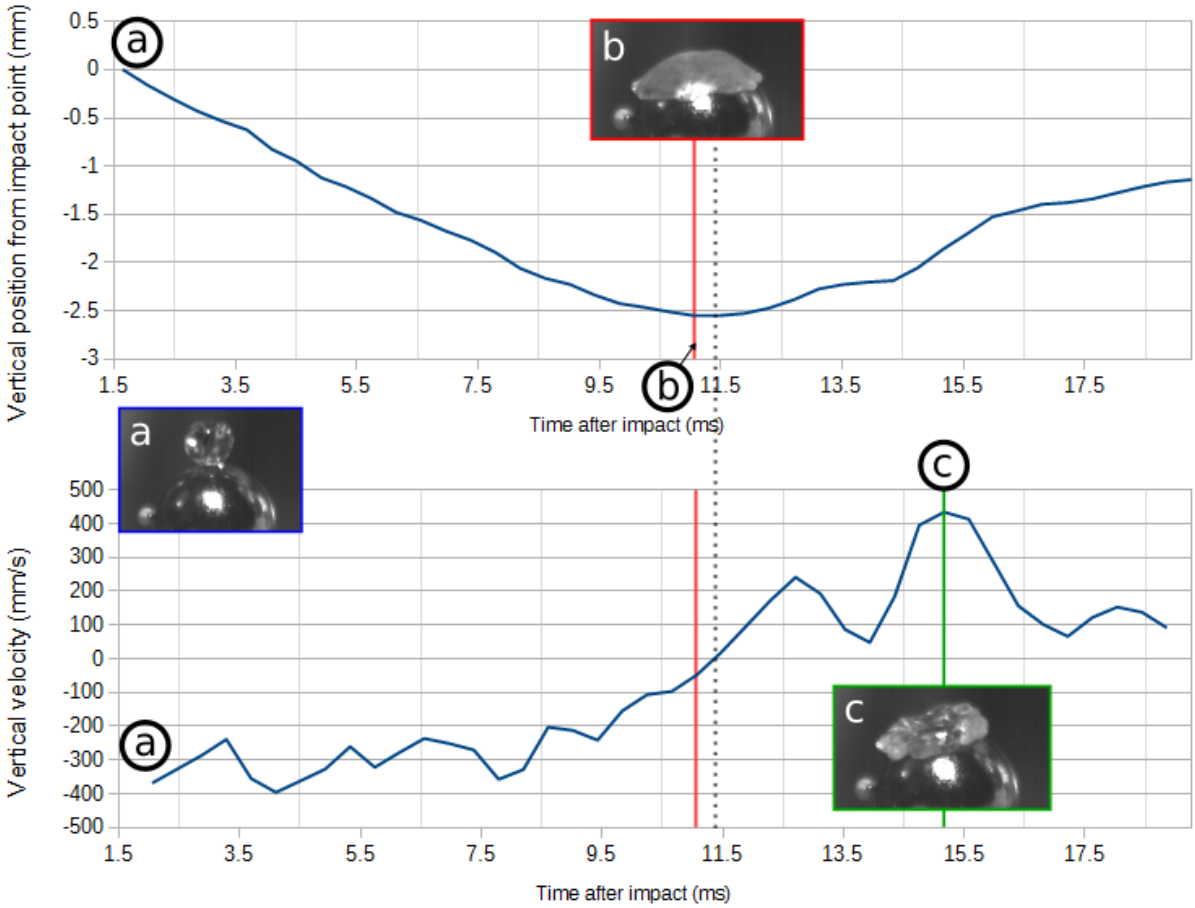

Figure 3.10. The vertical position and velocity of the drop's contact line (corresponding with Fig. 3.9). Three important stages of the process are shown as (a) initial impact, (b) hole formation, and (c) maximum hole diameter.

Figure 3.10 shows that the hole formation (solid red vertical line, b) occurrence at 0.4 ms before the time of maximum diameter (dotted black vertical line). A hole grows to a size of approximately 3.0 mm before closing. The green time mark corresponds with the maximum hole diameter as well as the maximum vertical velocity of the contact line.

3.3.3 Toroid

Toroids were defined as drops in which the hole continued to grow resulting in a torus. The toroids were characterized by their discrete break-up into a smaller number of finite drops. Toroids were formed for impinging drops ($d = 4.78$ mm) with Weber numbers from 15 to 30 at temperatures between 195 and 220 °C.

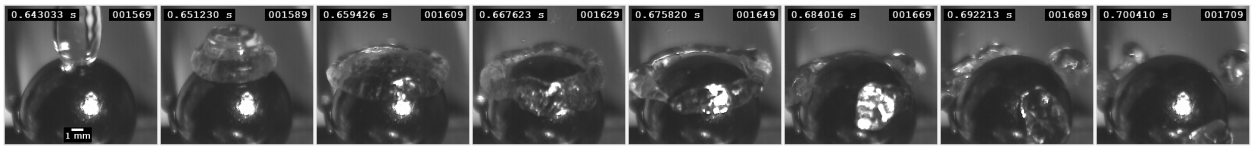

Figure 3.11. An impinging drop at a Weber number of 15.0 and surface temperature of 220°C. A hole forms in the drop and continues to grow until a toroid is formed. After formation the toroid breaks into smaller drops. This process is attributed to a Plauteau-Rayleigh type instability.

The elapsed time between drop impact and the formation of a hole was measured using Tracker. This was done for the toroid formation regime. Figure 3.12 shows the dimensionless hole formation time for Weber numbers from 15 to 30.

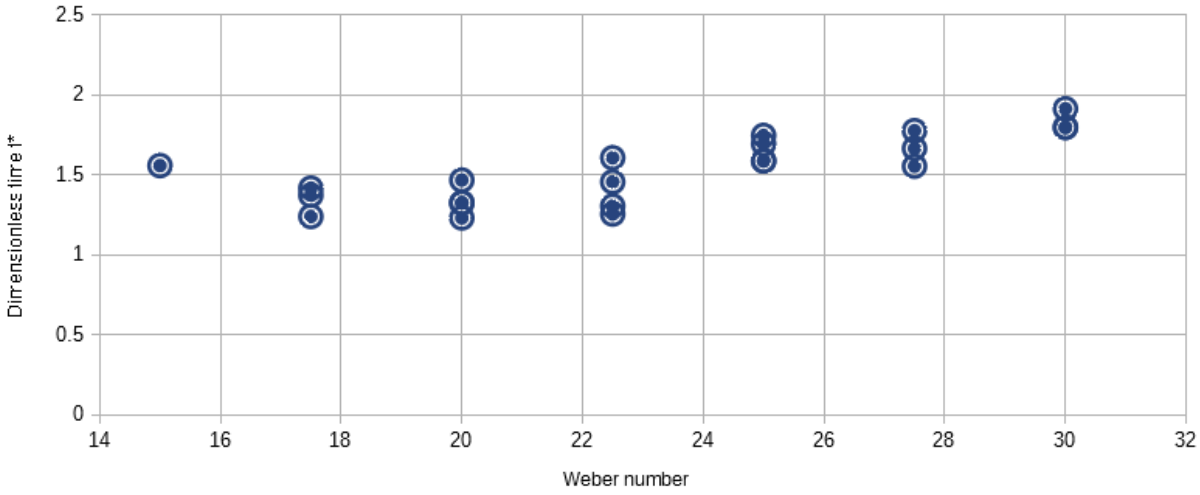

Figure 3.12. Time from drop impact to hole formation for Weber numbers (15 to 30) in toroids.

The liquid surface of the toroids exhibited wavelike patterns prior to breaking up into a discrete number of drops. Figure 3.13 shows the evolution of a toroid after drop impingement. The toroid subsequently broke up into four discrete drops. The maximum spreading diameter was measured with Tracker.

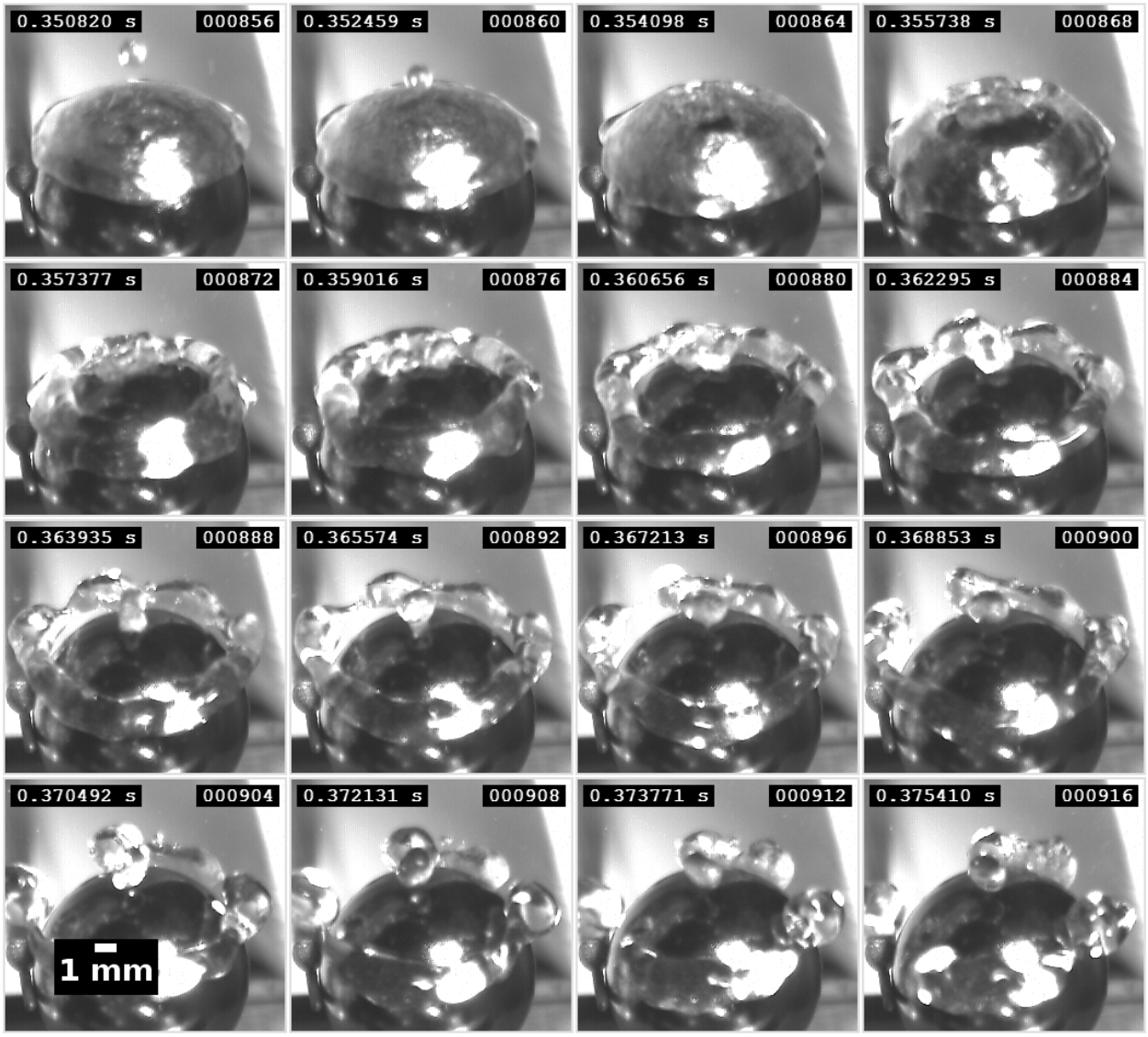

Figure 3.13. An impacting drop ($We = 30$; $T = 220$ °C) forms a torus which breaks into four smaller drops in a time frame of ~10 ms.

Following Wu (2003) [36], the geometric properties of a liquid torus can be related to the Weber number of the impinging drop. The major (c) and minor (a) radii (Fig. 1.8) of selected toroids were measured using Tracker for comparison with (1.7).

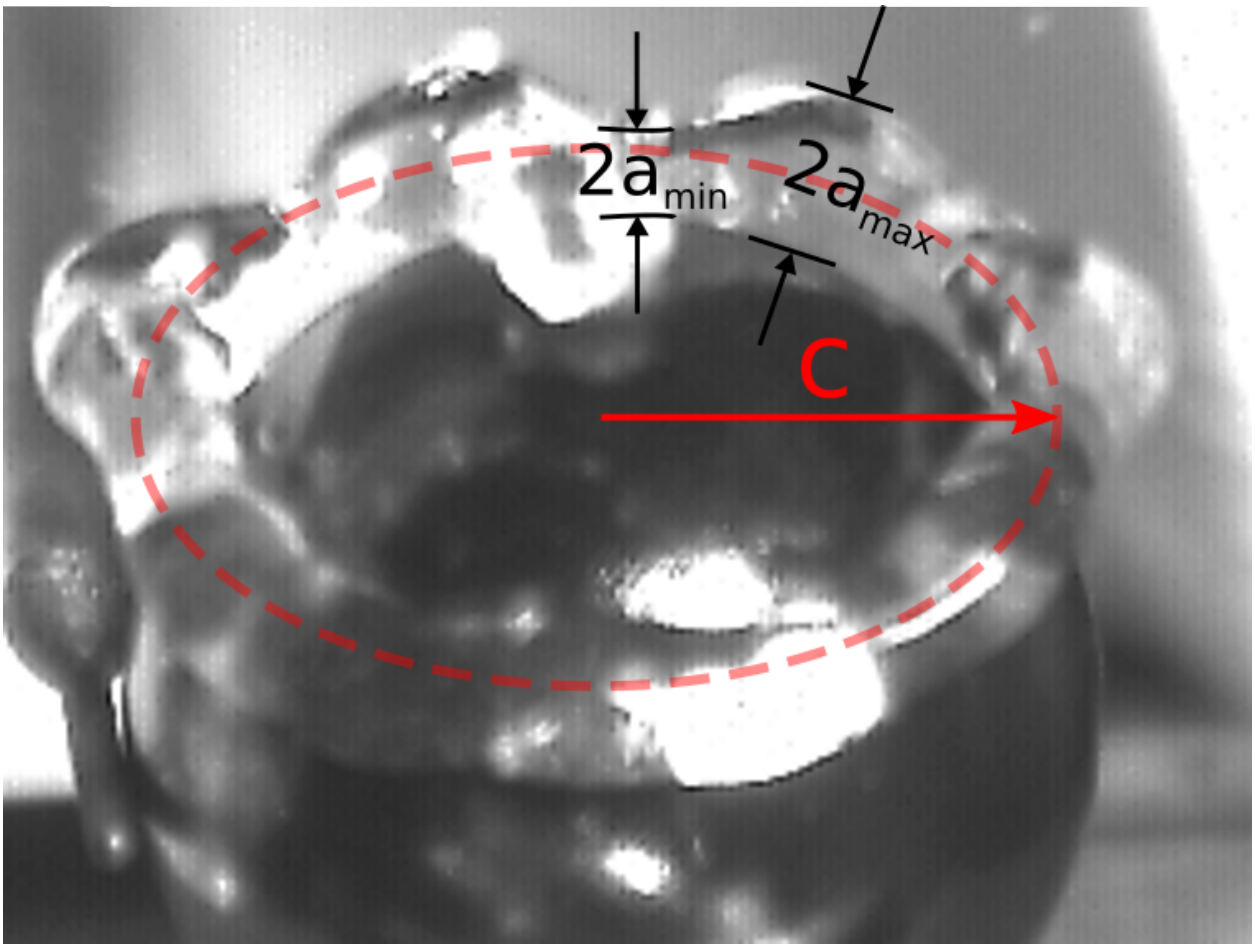

Figure 3.14. Close-up view of a torus (~5 ms after forming), shows characteristics of a Plateau-Rayleigh type instability. The parameters a and c represent the minor radius and major radius of the torus, respectively. The minimum and maximum minor radii are shown for completeness.

3.4 Analysis and Discussion

For the comparison between planar and spherical targets, the deviations in surface area measurements for the spherical targets might be attributed to irregularities in the spreading of the drop and the measurement method. Additional error is associated with the calculation of the spherical cap area by measuring the parameter h. A measurement of the maximum spreading diameter might reduce the associated standard deviation in the error. Despite these concerns, we conclude that the contact area over a spherical target is greater than that of a planar surface.

The 95% confidence interval bounds which were found for a and b in (3.1) are large. This is due to a relatively low number of data points used in the analysis. The decreasing direction of the observed residence time differs from models [4], which all tend toward an increase in residence time with higher Weber number. In this case, the critical Weber number was between 21.4 and 22.8.

In cases such as in Figure 3.8 for hole formation and closure, energy is lost. The hole breaks the surface tension at the top of the film. This surface energy in the toroid is responsible for its recollection into a single drop. In the middle part of the sequence the formation of a hole results in fragmentation, indicating lost energy.

The maximum spreading diameter and time for toroid formation at various Weber numbers was measured and compared to previous published models in Mitra et al. (2016) [15] and Araki and Moriyama (1981) [34]. The diameter was measured at the time of visible hole formation. This time scale represents that of the rupture of the fluid film.

Figure 3.15 shows the resulting comparison between the measured spread diameter and the values predicted by the models. A hole is formed after the maximum spreading diameter has been exceeded. This is evident in all cases in the study, except at a high Weber number (30).

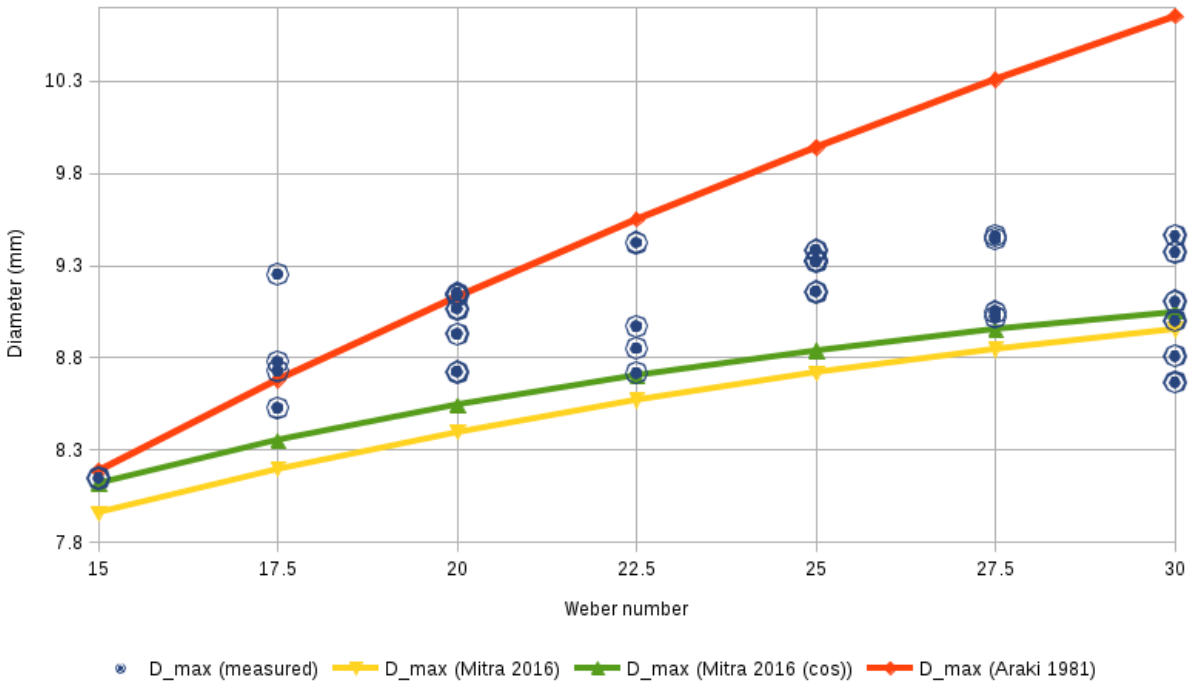

Figure 3.15. Measured and computed maximum spreading diameter in terms of Weber number.

Figure 3.15 includes a modified model "D_max (Mitra 2016 (cos))." In this model the peripheral surface area energy term was approximated by the sine of the half spread angle. From geometry, this factor represents the horizontal component of the film thickness at the point of maximum spreading. However, the vertical component of the film thickness is better representative of the given model's geometry from mass conservation considerations. Therefore this term in the model was modified to the cosine of the half spread angle. The results from this modified model show better agreement with experimental data. The root mean squared deviation (RMSD) between the models and the measurements were found to be as 0.93 mm, 0.51 mm, and

0.41 mm for Araki and Moriyama (1981) [34], Mitra (2016) [15], and Mitra (2016) [15] with cosine modification, respectively.

From mass conservation, the volume of the torus can be equated to the volume of the impinging drop:

$$m_1 = m_2 \Rightarrow \rho V_1 = \rho V_2 \Rightarrow \frac{\pi}{6} d_0^3 = 2\pi^2 a^2 c, \tag{3.2}$$

where a and c are the minor and major radii, respectively (see Fig. 1.8). The major diameter D (=$2c$) was measured using Tracker. This was compared to (1.6) given by Wu (2003) [36]. Following Wu (2003) [36], the minimum sectional diameter d_{se} (=$2a$) was calculated using (1.7) and compared to the measured minor radius a in Table 3.2.

Table 3.2. Measured and computed torus parameters.

We	D (measured) (mm)	D (Wu [36]) (mm)	Difference (%)	a (measured) (mm)	a (Wu [36]) (mm)	Difference (%)
15	8.454	11.615	27.2%	0.828	0.701	15.3%
15	9.287	11.615	20.0%	0.790	0.701	11.2%
20	8.583	16.316	47.4%	0.822	0.592	28.0%
25	9.172	21.813	58.0%	0.795	0.512	35.6%
30	8.513	28.106	69.7%	0.825	0.451	45.4%
30	9.196	28.106	67.3%	0.794	0.451	43.2%

Wu (2003) [36] also provides an approximate relationship for the diameter of the resulting drops after the toroid break-up:

$$d_s \approx \frac{1.25 d_l}{1 + \frac{We}{12}}. \tag{3.3}$$

Assuming that mass loss due to secondary atomization after impingement is negligible, conservation of mass can be used to approximate the volume of n number of discrete drops after the break-up:

$$\frac{\pi}{6} d_0^3 = n \frac{\pi}{6} d_s^3, \tag{3.4}$$

from which each drop's volume should be equal to the initial drop volume divided by n. A comparison between Wu (2003) [36] and (3.4) was performed and the difference is tabulated in Table 3.3. This model does not account for impact on a spherical geometry, evaporation, and dissipation, which may be sources of the discrepancy.

Table 3.3. Drop size: toroid break-up.

Weber Number	Difference (4 drops)	Difference (5 drops)	Difference (6 drops)
15	31.41%	14.27%	-2.88%
20	58.80%	48.50%	38.20%
25	73.35%	66.69%	60.02%
30	81.78%	77.22%	72.67%

The differences between the measured and computed toroid major diameters from (1.6), as well as the differences in drop sizes, increase with Weber number. A possible explanation is that Wu (2003) [36] neglects potential energy by assuming a planar surface. The difference in vertical distance between the center of mass of the undeformed drop and the toroid is assumed to be negligible compared to the kinetic energy. Another possible source of discrepancy may be rotation and fluid motion of the toroid. It was observed in the high speed videos that the toroids had a nonzero angular velocity. The model given by Wu (2003) [36] does not account for internal fluid motion and any dissipative effects. These assumptions may be partially responsible for the differences in the calculated major toroid diameters.

For liquid jet flows, the Plateau-Rayleigh linear stability analysis may be used to find the perturbation or wavelength which grows fastest and leads to break-up. This can be calculated for the jet as $kR_0 = 0.697$, which may be solved for this wavelength with $k = \frac{2\pi}{\lambda}$ yielding $\lambda_{max} \approx 9.02R_0$ [45]. From conservation of mass (3.2), the measured major diameter of the toroid is used to determine its unperturbed minor radius a which will be assumed to be R_0 in this case. Table 3.4 shows the measured and calculated critical wavelength values.

Table 3.4. Measured and computed critical wavelength.

We	D (measured) (mm)	R_0 (mass cons.) (mm)	λ_{max} (measured) (mm)	λ_{max} (calculated) (mm)	Difference (%)
15	8.454	0.828	4.742	7.467	36.5%
15	9.287	0.790	4.426	7.125	37.9%
20	8.583	0.822	4.142	7.411	44.1%
25	9.172	0.795	4.374	7.169	39.0%
30	8.513	0.825	4.304	7.441	42.2%
30	9.196	0.794	4.197	7.160	41.4%

The calculated wavelength was found to be consistently larger than the measured wavelength by a factor of ~1.7; less than an order of magnitude in difference indicating that it is more of a first

order approximation. One experimental consideration was the method used to measure the wavelength of the perturbation through image analysis. Ideally, the camera might have been positioned directly above the target perpendicular to the horizontal plane. This top-down view would reduce any skewing of the image. In our case, the resulting angles made the determination of the wavelengths subject to a relatively large error. The low standard deviation in measured wavelength ($SD = 0.21$) indicates skewing of the image might have been a factor.

Another consideration is the difference between toroidal and cylindrical jet geometries and fluid dynamics. Table 3.5 is a comparison between the circumference C of the toroid with respect to the measured and calculated critical wavelengths.

Table 3.5. Circumference for measured and calculated critical wavelengths.

We	D (measured) (mm)	C (derived) (mm)	$\frac{C}{\lambda_{max}}$ (measured λ_{max}) (mm/mm)	$\frac{C}{\lambda_{max}}$ (calculated λ_{max}) (mm/mm)
15	8.454	26.559	5.601	3.557
15	9.287	29.176	6.592	4.095
20	8.583	26.964	6.510	3.638
25	9.172	28.815	6.588	4.019
30	8.513	26.744	6.214	3.594
30	9.196	28.890	6.884	4.035
Mean:	8.868	27.858	6.398	3.823
Standard deviation:	0.388	1.220	0.445	0.251

The mean number of waves measured per toroid was 6.40 ± 0.45. The observed number of secondary drops formed after toroid break-up was 4.17 ± 0.41. The resulting visible and measured perturbation wavelengths were approximate and may not be the actual critical wavelengths. Furthermore, the mean number of waves per toroid found by dividing the circumference of the toroid by the calculated critical perturbation wavelength was 3.82 ± 0.25. Notably, this coincides with the number of secondary drops. Higher precision measurements combined with more advanced analysis of the perturbation components may provide more accurate critical wavelength values.

3.5 Packed Bed Target

A supplementary study of the impingement of a liquid drop on a substrate of multiple smaller solid spheres was performed. Situations in which the impinging drops engulf a catalyst substrate in FCC processes can have a negative impact on the system's output by reducing its efficiency [15]. In this experiment, a bed of small spherical particles of diameters ranging from

1.0 mm to 2.0 mm was heated to a temperature of 250 °C. Liquid water drops were impinged onto the target for Weber numbers from 10 to 45.3.

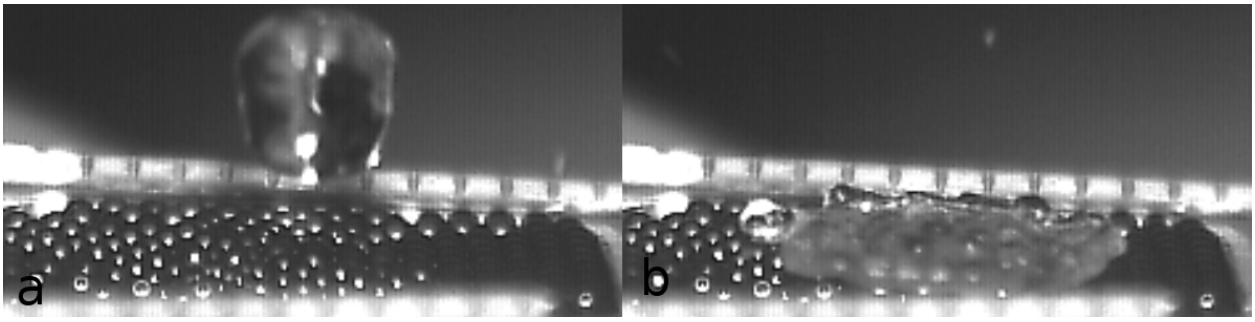

Figure 3.16. Impingement of a drop ($d = 4.78$ mm; $We = 45.3$) on a sphere substrate ($d = 1.0$ mm; T=250°C) (a) before impact, and (b) after impact.

In these cases, the drops did not exhibit the traditional Leidenfrost behavior of strictly rebounding or break-up upon impact. Instead, the drops appeared to contact the substrate in the transition boiling regime and continue to boil in this regime for a significant amount of time. In this regime, the drops appeared to engulf the particles upon impingent. After a duration (~0.2 s), the drop stabilized and exhibited a transition to film boiling. This transition had minimal drop movement. The drop was quasi-stationary until it fully evaporated. The elapsed time between impact and the transition to film boiling was denoted as “settling time” as shown in Figure 3.17.

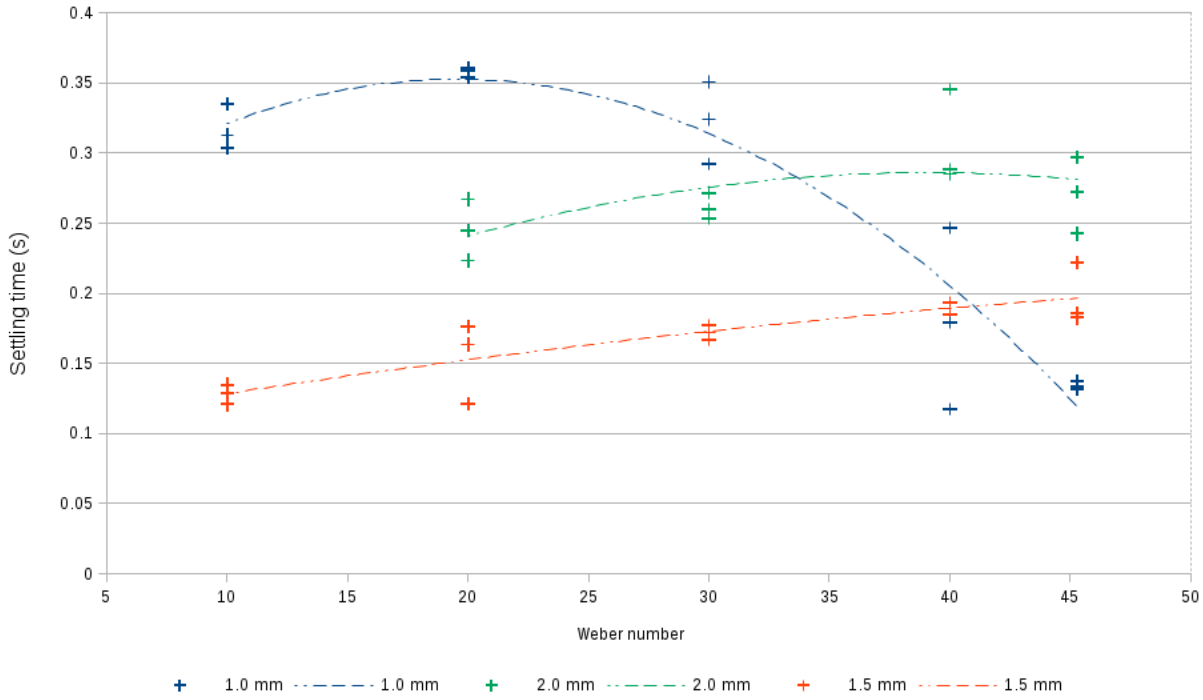

Figure 3.17. Settling time for drops on 1.0, 1.5, and 2.0 mm spherical packed beds at 220 °C for Weber numbers from 10 to 45.3.

For the substrates composed of 1.5 and 2.0 mm diameters, the settling time increased with impacting Weber number, with an observed inflection at higher Weber numbers. For 1.0 mm diameter substrates, it was seen that the settling time had an apparent inflection point at a much lower Weber number (20). A possible explanation for this effect follows from a thermodynamic perspective. As the drop impinges upon the substrate, it appears to be in the transition boiling regime. In this regime, heat flux is still relatively higher than in the film boiling regime, allowing the drop to absorb the heat of the small spheres it engulfs. After a sufficient amount of heat is transferred, the engulfed spheres obtained thermal equilibrium with the liquid. However, the surrounding spheres near the outer surface of the drop are assumed to be at a temperature sufficient to maintain film boiling.

Another interesting phenomenon often associated with bubbles and drops is the formation of liquid jets. During image analysis it was seen that a single liquid jet (Figure 3.18) was formed immediately before impact on a packed bed. In this case, the spheres in the substrate had a diameter of 1.0 mm. The impinging drop had a diameter of 4.78 mm and a Weber number of 20. Using Tracker, the jet was measured to have a vertical velocity of 4.32 m/s at formation compared to the drop's measured vertical velocity of 0.51 m/s.

Figure 3.18. Liquid jet formation.

4 CONCLUSION AND FUTURE WORK

4.1 Conclusion

The impingement of water drops on planar and spherical surfaces was studied for Weber numbers between 10 and 45.3 for target temperatures between 160 °C and 220 °C. A versatile and custom experimental system was designed to efficiently heat metal targets above their Leidenfrost point. This system included the application of microcontrollers and electrical circuits for closed-loop feedback control. A custom positioning system using linear optical stages allowed for spatial adjustments on the order of micrometers. It was found that a drop spreads over a greater surface area on a sphere than on a planar surface for the same Weber number. It was also found that the ratio of the drop diameter to target diameter influences the Leidenfrost temperature. Four distinct regimes were observed for the impacts on spherical targets:

- **Rebounding**
- **Hole Formation**
- **Toroid Formation**
- **Non-toroidal Break-up**

The dimensionless residence time was found to have a negligible impact on the studied regimes. A critical Weber number separated the rebounding regime and hole formation. Toroids may be formed beyond this critical Weber number. The geometric properties of the toroids were measured and compared to existing theory for impacts on planar surfaces which showed discrepancy between the target geometries. The break-up of the toroids was shown to exhibit a Plateau-Rayleigh type instability. The critical perturbation wavelength in the toroids was measured and analyzed. The results from existing models showed that the critical wavelength for break-up was similar to that for cylindrical geometries, whereas the measured critical wavelength did not coincide with observations.

4.2 Future Work

A number of improvements might be made for further study. One such improvement is an analytical model for prediction of the toroid formation as a function of the Weber number. Larger parameter ranges for surface temperatures, aspect ratios, and Weber numbers could also support a more complete study. Novel data might also be acquired through the use of near infrared (NIR) photography to better quantify water vapor content. A hypothetical extrapolation of data obtained for Figure 3.5 was used in Figure 4.1 for higher Weber numbers and surface temperatures.

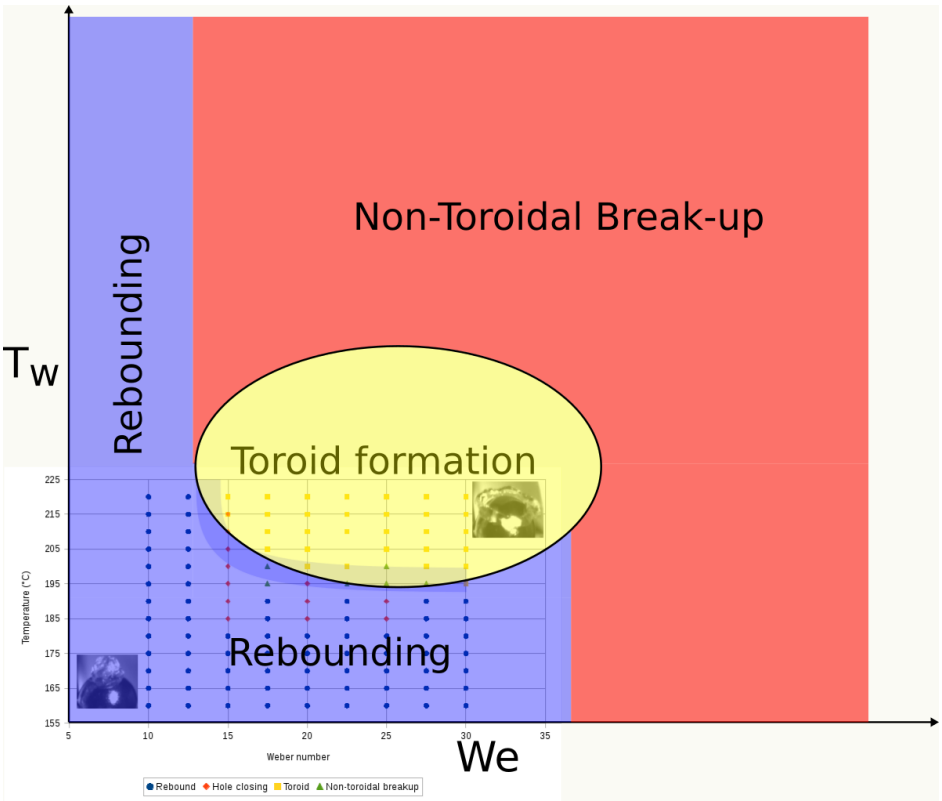

Figure 4.1. Hypothesized toroidal formation regime surrounded by rebounding and non-toroidal break-up regimes for a greater range of temperatures and Weber numbers.

The analytical model given by Mitra et al. (2016) [15] could be expanded to include the formation of a hole. The addition of a hole formation in the model might follow with the assumption that the hole (at the north pole of the sphere) would have a diameter of a vapor bubble for the regime being studied [46]. This diameter could be added to the spherical geometry and a similar equation derived to attempt to relate hole formation to non-dimensional parameters. Figure 4.2 shows a diagram of the proposed model geometry over an image acquired at the time of hole formation.

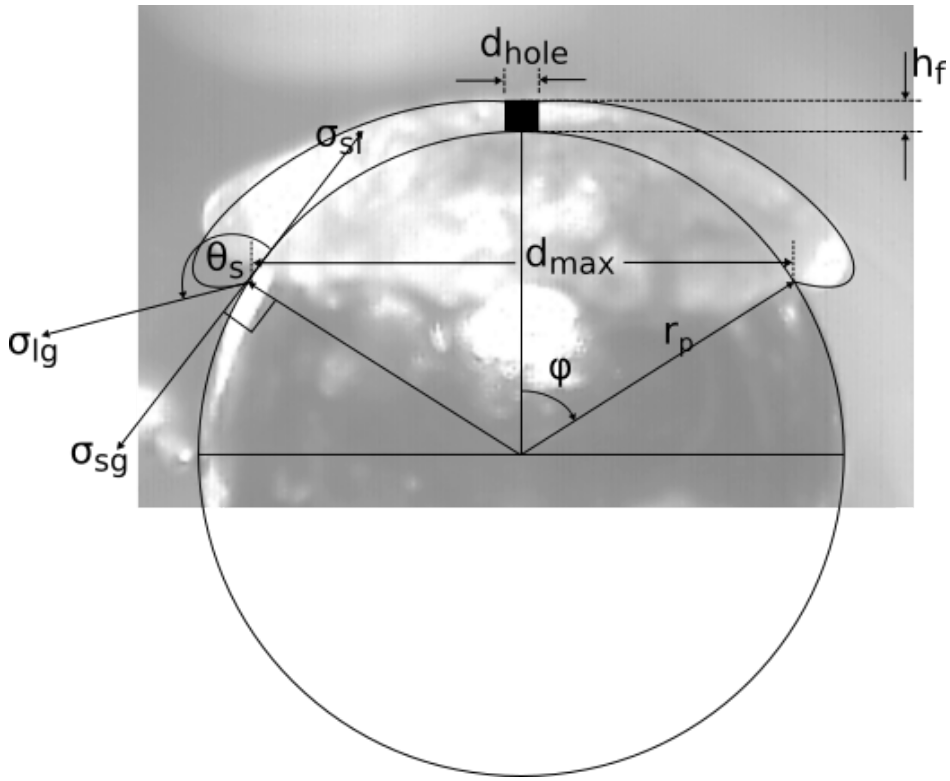

Figure 4.2. The geometry for a proposed energy balance model including vapor bubble formation.

Further study into the effects of drop impingement on a packed bed is needed. An analysis from a heat transfer perspective may provide insight as to why the drops initially boil and then settle. Additional thermocouples could be added at various spatial locations in the bed and monitored to observe changes in temperature.

An emerging tool for optical analysis is near-infrared (NIR) photography. In recent years, this form of photography has experienced a boom in productivity, in part due to technological advances in optics such as mirrorless cameras which have made it less costly and more accessible [47]. Near-infrared photography is especially useful for visualizing particles which absorb or reflect more in the near-infrared region of the electromagnetic spectrum, such as water vapor. It can also be used to eliminate visible ambient light concerns. An exploratory investigation was performed using a Sony α5000 mirrorless digital camera converted by LifePixel Infrared (Mukilteo, WA) for a wavelength of 830 nm. A sphere ($d = 9.56$mm) was heated (220 °C) and a drop ($We = 171$) was impinged on its surface. This resulting long-exposure image (Fig. 4.3) shows the water vapor trails from small fragments ejected by the drop's impact.

Figure 4.3. Long-exposure, near-infrared photography of a drop impinging on a heated surface reveals water vapor trails of drop fragments.

Appendix A CONVECTION CALCULATIONS

A qualitative analysis of convective heat transfer using Newton's law of cooling ($\dot{Q} = hA(T_s - T_f)$) was attempted. First, it was assumed that the heat flux due to conduction and radiation are equal in each situation, which allowed us to focus solely on convection. Second, the assumption that the heat flux between a reference state 1 and the state to be compared 2 was equal ($\dot{Q}_1 = \dot{Q}_2$), and the only variation between the two states was a difference in surface area in contact with the impinging drop. In this case, the difference was due to an increase in the drop diameter at state 2. A further assumption that was made was that the spreading diameter of the drop upon impingement on the target increased with increasing drop diameter. From the geometry of a sphere given in Figure 3.1, the surface area of the spherical cap was defined as $A = 2\pi rh$, where r is the radius of the target sphere and h is the vertical distance from the top of the sphere to the spreading diameter line. Lastly, it was assumed that the temperature of the impinging drop remains constant.

Equating the heat flux of both states,

$$hA_1(T_{s1} - T_f) = hA_2(T_{s2} - T_f) \tag{A.1}$$

and then solving for the surface temperature at state 2 yields

$$T_{s2} = \frac{A_1}{A_2}(T_{s1} - T_f) + T_f. \tag{A.2}$$

At this point it can be seen that as the area is increased at state 2, the resulting Leidenfrost temperature would be reduced as the ratio of areas between the two states is below unity. Substituting the definition of the surface area of a spherical cap into Eq. A.2 yields

$$T_{s2} = \frac{r_s - \sqrt{r_s^2 - a_1^2}}{r_s - \sqrt{r_s^2 - a_2^2}}(T_{s1} - T_f) + T_f \tag{A.3}$$

which again shows that under the assumption that spreading diameter (or radius a) at state 2 is greater than that of state 1, the resulting Leidenfrost temperature will be reduced. However it can be readily seen that this equation is only valid for spreading diameters less than or equal to that of the diameter of the target sphere. This result does not agree with the observations in Figure 3.3 and in fact seems to be the opposite. In the Figure, state 1 could be taken to be at the ratio of 0.6 and state 2 at 0.65. The resulting increase in Leidenfrost temperature observed compared to a predicted reduction clearly shows that this qualitative analysis makes too many assumptions to accurately predict a given Leidenfrost temperature.

Appendix B TOROID MODEL

A model to attempt to predict the geometry of a torus was developed beginning with an energy conservation in a similar fashion to that performed by Mitra et al. (2016) [15]. First, conservation of energy is applied at both states:

$$E_1 = E_2 \tag{B.1}$$

At state 1, the drop is in contact with the spherical target but has not yet deformed. At state 1, the drop has both potential energy due to gravity and surface tension, and kinetic energy. At state 2, it is assumed that the drop no longer has kinetic energy and is in the form of a torus. In this state, the torus has potential energy due to gravity and surface tension. Substituting these terms into B.1 yields

$$E_{pg1} + E_{ps1} + E_{k1} = E_{pg2} + E_{ps2} \tag{B.2}$$

where the terms in state 1 are given as

$$\begin{aligned} E_{pg1} &= \rho V h_1 = \rho \frac{\pi}{6} d_0^3 \left(r_s + r_d\right) g \\ E_{ps1} &= \pi d_0^2 \sigma \\ E_{k1} &= \frac{\pi}{12} d_0^3 \rho v_0^2 \end{aligned} \tag{B.3}$$

where ρ, d_0, r_d, and v_0 are the liquid drop's density, initial diameter, initial radius, and initial velocity, respectively. The radius of the spherical target is given as r_s.

At state 2, the geometry of a ring torus is used (see Figure 1.8). It is further assumed that the toroid rests upon the spherical target. The energy terms at state 2 are then given as

$$\begin{aligned} E_{pg2} &= 2\rho g \pi^2 a^2 c \sqrt{\left(r_s + a\right)^2 - c^2} \\ E_{ps2} &= 4\pi^2 ac\sigma. \end{aligned} \tag{B.4}$$

Substituting (B.3) and (B.4) into (B.2) and normalizing each term by the potential energy due to surface tension at state 1 yields

$$\frac{1}{6} Bo + 1 + \frac{1}{12} We = \frac{2\rho g \pi a^2 c \sqrt{\left(r_s + a\right)^2 - c^2}}{d_0^2 \sigma} + \frac{4\pi ac}{d_0^2} \tag{B.5}$$

where Bo and We are the drop's Bond and Weber numbers, respectively. For the Bond number, the characteristic length is assumed to be $L = \sqrt{d_0 \left(r_s + r_d\right)}$.

Next, conversation of mass is applied between the two states:

$$m_1 = m_2 \Rightarrow \rho V_1 = \rho V_2 \Rightarrow \frac{\pi}{6} d_0^3 = 2\pi^2 a^2 c \tag{B.6}$$

In this model, neither a nor c of the toroid are known a-priori and (B.5) and (B.6) must be solved simultaneously using iterative methods.

While the model appears geometrically acceptable, the solutions of the model found through the use of numerical solvers are often complex or trivial. A check was performed to verify the ratio of energy and mass at both states, both of which were found to be sufficiently close to unity only for trivial solutions. This is suggestive of the existence of nonzero energy terms which have been neglected at the final state. While viscous dissipation is expected to be nonzero, the contribution of a term including the toroid's angular velocity is expected to be greater. As a result of these missing terms, the measured data were unable to be compared to the model in its current state.

NOTES

Bibliography

[1] Leidenfrost, Johann Gottlob. “On the fixation of water in diverse fire”. en. In: *International Journal of Heat and Mass Transfer* 9.11 (Nov. 1966), pp. 1153–1166. ISSN: 00179310. DOI: 10.1016/0017-9310(66)90111-6.

[2] Geraldi, Nicasio R. et al. “Leidenfrost transition temperature for stainless steel meshes”. en. In: *Materials Letters* 176 (Aug. 2016), pp. 205–208. ISSN: 0167577X. DOI: 10.1016/j.matlet.2016.04.124.

[3] Quéré, David. “Leidenfrost Dynamics”. en. In: *Annual Review of Fluid Mechanics* 45.1 (Jan. 2013), pp. 197–215. ISSN: 0066-4189, 1545-4479. DOI: 10.1146/annurev-fluid-011212-140709.

[4] Liang, Gangtao and Mudawar, Issam. “Review of drop impact on heated walls”. en. In: *International Journal of Heat and Mass Transfer* 106 (Mar. 2017), pp. 103–126. ISSN: 00179310. DOI: 10.1016/j.ijheatmasstransfer.2016.10.031.

[5] Vakarelski, Ivan U. et al. “Leidenfrost Vapor Layers Reduce Drag without the Crisis in High Viscosity Liquids”. In: *Phys. Rev. Lett.* 117 (11 Sept. 2016), p. 114503. DOI: 10.1103/PhysRevLett.117.114503.

[6] Walker, Jearl. “Drops of water dance on a hot skillet and the experimenter walks on hot coals”. In: *Scientific American* 237.2 ().

[7] Börnhorst, M. and Deutschmann, O. “Single droplet impingement of urea water solution on a heated substrate”. en. In: *International Journal of Heat and Fluid Flow* 69 (Feb. 2018), pp. 55–61. ISSN: 0142727X. DOI: 10.1016/j.ijheatfluidflow.2017.10.007.

[8] Ng, Boon T., Hung, Yew M., and Tan, Ming K. “Suppression of the Leidenfrost effect via low frequency vibrations”. en. In: *Soft Matter* 11.4 (2015), pp. 775–784. ISSN: 1744-683X, 1744-6848. DOI: 10.1039/C4SM02272F.

[9] Ng, Boon T., Hung, Yew Mun, and Tan, Ming K. “Acoustically-controlled Leidenfrost droplets”. en. In: *Journal of Colloid and Interface Science* 465 (Mar. 2016), pp. 26–32. ISSN: 00219797. DOI: 10.1016/j.jcis.2015.11.047.

[10] Wciślik, Sylwia. “Thermal infrared mapping of the Leidenfrost drop evaporation”. In: *Thermal infrared mapping of the Leidenfrost drop evaporation*. Vol. 032064. 745. 2016. DOI: 10.1088/1742-6596/745/3/032064.

[11] Bernardin, J. D. and Mudawar, I. “The Leidenfrost Point: Experimental Study and Assessment of Existing Models”. en. In: *Journal of Heat Transfer* 121.4 (1999), p. 894. ISSN: 00221481. DOI: 10.1115/1.2826080.

[12] Gunnerson, F. S. and Yackle, T. R. “Quenching and Rewetting of Nuclear Fuel Rods”. In: *Nuclear Technology* 54.1 (1981), pp. 113–117. DOI: 10.13182/NT81-A32759. eprint: https://doi.org/10.13182/NT81-A32759.

[13] Berthoud, Georges. “Vapor Explosions”. en. In: (), pp. 573–611.

[14] Clough, Melissa et al. “Nanoporous materials forge a path forward to enable sustainable growth: Technology advancements in fluid catalytic cracking”. In: *Microporous and Mesoporous Materials* 254 (2017). Zeolites for a Sustainable World, pp. 45–58. ISSN: 1387-1811. DOI: https://doi.org/10.1016/j.micromeso.2017.03.063.

[15] Mitra, Subhasish et al. “On wetting characteristics of droplet on a spherical particle in film boiling regime”. en. In: *Chemical Engineering Science* 149 (July 2016), pp. 181–203. ISSN: 00092509. DOI: 10.1016/j.ces.2016.04.003.

[16] Baktash, Mehri. “Jumping Leidenfrost Droplets”. PhD thesis. Lund, 2012.

[17] Chen, Meng-yao et al. “Self-propulsion of Leidenfrost droplets on micropillared hot surfaces with gradient wettability”. en. In: *Applied Surface Science* 433 (Mar. 2018), pp. 336–340. ISSN: 01694332. DOI: 10.1016/j.apsusc.2017.10.033.

[18] Grounds, Alex, Still, Richard, and Takashina, Kei. “Enhanced Droplet Control by Transition Boiling”. en. In: *Scientific Reports* 2.1 (Dec. 2012). ISSN: 2045-2322. DOI: 10.1038/srep00720.

[19] Maquet, L. et al. “Leidenfrost drops: Effect of gravity”. en. In: *EPL (Europhysics Letters)* 110.2 (Apr. 2015), p. 24001. ISSN: 0295-5075, 1286-4854. DOI: 10.1209/0295-5075/110/24001.

[20] Huang, Chen-Kang and Carey, Van P. “The effects of dissolved salt on the Leidenfrost transition”. en. In: *International Journal of Heat and Mass Transfer* 50.1-2 (Jan. 2007), pp. 269–282. ISSN: 00179310. DOI: 10.1016/j.ijheatmasstransfer.2006.06.031.

[21] Chen, Hua et al. “Dynamic Leidenfrost temperature increase of impacting droplets containing high-alcohol surfactant”. en. In: *International Journal of Heat and Mass Transfer* 118 (Mar. 2018), pp. 1160–1168. ISSN: 00179310. DOI: 10.1016/j.ijheatmasstransfer.2017.11.100.

[22] Raufaste, C., Bouret, Y., and Celestini, F. “Reactive Leidenfrost droplets”. en. In: *EPL (Europhysics Letters)* 114.4 (May 2016), p. 46005. ISSN: 0295-5075, 1286-4854. DOI: 10.1209/0295-5075/114/46005.

[23] Banitabaei, S. A. and Amirfazli, A. “Droplet impact onto a solid sphere: Effect of wettability and impact velocity”. en. In: *Physics of Fluids* 29.6 (June 2017), p. 062111. ISSN: 1070-6631, 1089-7666. DOI: 10.1063/1.4990088.

[24] Gradeck, M. et al. “Heat transfer for Leidenfrost drops bouncing onto a hot surface”. en. In: *Experimental Thermal and Fluid Science* 47 (May 2013), pp. 14–25. ISSN: 08941777. DOI: 10.1016/j.expthermflusci.2012.10.023.

[25] Breitenbach, Jan, Roisman, Ilia V., and Tropea, Cameron. “Heat transfer in the film boiling regime: Single drop impact and spray cooling”. en. In: *International Journal of Heat and Mass Transfer* 110 (July 2017), pp. 34–42. ISSN: 00179310. DOI: 10.1016/j.ijheatmasstransfer.2017.03.004.

[26] Rueda Villegas, Lucia et al. “Direct numerical simulation of the impact of a droplet onto a hot surface above the Leidenfrost temperature”. en. In: *International Journal of Heat and Mass Transfer* 104 (Jan. 2017), pp. 1090–1109. ISSN: 00179310. DOI: 10.1016/j.ijheatmasstransfer.2016.08.105.

[27] Biance, Anne-Laure, Pirat, Christophe, and Ybert, Christophe. “Drop fragmentation due to hole formation during Leidenfrost impact”. en. In: *Physics of Fluids* 23.2 (Feb. 2011), p. 022104. ISSN: 1070-6631, 1089-7666. DOI: 10.1063/1.3553277.

[28] Moon, Joo Hyun, Cho, Minhaeng, and Lee, Seong Hyuk. “Dynamic wetting and heat transfer characteristics of a liquid droplet impinging on heated textured surfaces”. en. In: *International Journal of Heat and Mass Transfer* 97 (June 2016), pp. 308–317. ISSN: 00179310. DOI: 10.1016/j.ijheatmasstransfer.2016.02.041.

[29] Clavijo, Cristian E., Crockett, Julie, and Maynes, Daniel. “Hydrodynamics of droplet impingement on hot surfaces of varying wettability”. en. In: *International Journal of Heat and Mass Transfer* 108 (May 2017), pp. 1714–1726. ISSN: 00179310. DOI: 10.1016/j.ijheatmasstransfer.2016.12.076.

[30] Lee, Gi Cheol et al. “Induced liquid-solid contact via micro/nano multiscale texture on a surface and its effect on the Leidenfrost temperature”. en. In: *Experimental Thermal and Fluid Science* 84 (June 2017), pp. 156–164. ISSN: 08941777. DOI: 10.1016/j.expthermflusci.2017.01.022.

[31] Bakshi, Shamit, Roisman, Ilia V., and Tropea, Cam. “Investigations on the impact of a drop onto a small spherical target”. en. In: *Physics of Fluids* 19.3 (Mar. 2007), p. 032102. ISSN: 1070-6631, 1089-7666. DOI: 10.1063/1.2716065.

[32] Zhu, Yang et al. “Dynamics of drop impact onto a solid sphere: spreading and retraction”. en. In: *Journal of Fluid Mechanics* 824 (Aug. 2017). ISSN: 0022-1120, 1469-7645. DOI: 10.1017/jfm.2017.388.

[33] Mitra, Subhasish et al. “Droplet impact dynamics on a spherical particle”. en. In: *Chemical Engineering Science* 100 (Aug. 2013), pp. 105–119. ISSN: 00092509. DOI: 10.1016/j.ces.2013.01.037.

[34] Araki, Kazuo and Moriyama, Akira. “Theory on deformation behavior of a liquid droplet impinging onto hot metal surface.” en. In: *Transactions of the Iron and Steel Institute of Japan* 21.8 (1981), pp. 583–590. ISSN: 0021-1583, 1881-1183. DOI: 10.2355/isijinternational1966.21.583.

[35] Lautrup, Benny. *Physics of Continuous Matter*. Jan. 2004.

[36] Wu, Z.-N. “Approximate critical Weber number for the breakup of an expanding torus”. eng. In: *Acta Mechanica* 166.1 (Dec. 2003), pp. 231–239. ISSN: 0001-5970.

[37] Mcgraw, Joshua D. et al. “Plateau-Rayleigh instability in a torus: formation and breakup of a polymer ring”. In: *Soft Matter* 6.6 (Mar. 2010), pp. 1258–1262. ISSN: 1744-683X.

[38] A., Cengel Yunus and Cimbala, John M. *Fluid mechanics: fundamentals and applications*. McGraw Hill, 2014.

[39] Sengers, J. V. and Watson, J. T. R. “Improved International Formulations for the Viscosity and Thermal Conductivity of Water Substance”. eng. In: *Journal of Physical and Chemical Reference Data* 15.4 (Oct. 1986), pp. 1291–1314. ISSN: 0047-2689.

[40] Brown, Douglas. *Tracker Video Analysis and Modeling Tool*. May 2018.

[41] Schindelin, Johannes et al. “Fiji: an open-source platform for biological-image analysis”. In: *Nature Methods* 9.7 (June 2012). ISSN: 1548-7091.

[42] Schneider, Caroline A, Rasband, Wayne S, and Eliceiri, Kevin W. “NIH Image to ImageJ: 25 years of image analysis”. In: *Nature Methods* 9.7 (June 2012). ISSN: 1548-7091.

[43] Bunting Magnetics Europe Ltd. *”Characteristics of NdFeB Magnets”*. URL: https://e-magnetsuk.com/neodymium_magnets/characteristics.aspx (visited on 05/30/2018).

[44] Mills, Anthony F. *Heat Transfer*. 2nd ed. Prentice Hall, Inc., 1999.

[45] François, Charru and Forcrand-Millard, Patricia De. *Hydrodynamic instabilities*. Cambridge University Press, 2011.

[46] Gunnerson, F.S. and Cronenberg, A.W. “On the Minimum Film Boiling Conditions for Spherical Geometries”. en. In: *Journal of Heat Transfer* 102 (May 1980). ISSN: 0022-1481.

[47] Life Pixel Infrared. *”LifePixel Infrared Conversions, IR Modifications & Photography Tutorials”*. URL: `https://www.lifepixel.com/` (visited on 05/30/2018).